Remote Sensing of Environment 268 (2022) 112752

Contents lists available at ScienceDirect

Remote Sensing of Environment

journal homepage: www.elsevier.com/locate/rse

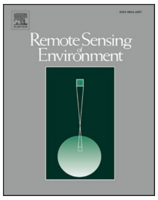

Remote sensing annual dynamics of rapid permafrost thaw disturbances with LandTrendr

Alexandra Runge [a,b,*], Ingmar Nitze [a], Guido Grosse [a,b]

[a] Alfred Wegener Institute Helmholtz Centre for Polar and Marine Research, Telegrafenberg A45, 14473 Potsdam, Germany
[b] Institute of Geosciences, University of Potsdam, Karl-Liebknecht-Str. 24-25, 14476 Potsdam, Germany

A R T I C L E I N F O

Edited by Dr. Menghua Wang

Keywords:
Retrogressive thaw slumps
Time series
Multi-spectral analysis
Landsat
Sentinel-2
Thermo-erosion
Permafrost thaw

A B S T R A C T

Permafrost is warming globally which leads to widespread permafrost thaw. Particularly ice-rich permafrost is vulnerable to rapid thaw and erosion, impacting whole landscapes and ecosystems. Retrogressive thaw slumps (RTS) are abrupt permafrost disturbances that expand by several meters each year and lead to an increased soil organic carbon release. Local Remote Sensing studies identified increasing RTS activity in the last two decades by increasing number of RTS or heightened RTS growth rates. However, a large-scale assessment across diverse permafrost regions and at high temporal resolution allowing to further determine RTS thaw dynamics and its main drivers is still lacking.

In this study we apply the disturbance detection algorithm LandTrendr for automated large-scale RTS mapping and high temporal thaw dynamic assessment to North Siberia ($8.1 \times 10^6 km^2$). We adapted and parametrised the temporal segmentation algorithm for abrupt disturbance detection to incorporate Landsat+Sentinel-2 mosaics, conducted spectral filtering, spatial masking and filtering, and a binary machine-learning object classification of the disturbance output to separate between RTS and false positives (F1 score: 0.609). Ground truth data for calibration and validation of the workflow was collected from 9 known RTS cluster sites using very high-resolution RapidEye and PlanetScope imagery.

Our study presents the first automated detection and assessment of RTS and their temporal dynamics at large-scale for 2001–2019. We identified 50,895 RTS and a steady increase in RTS-affected area from 2001 to 2019 across North Siberia, with a more abrupt increase from 2016 onward. Overall the RTS-affected area increased by 331% compared to 2000 (2000: 20,158 ha, 2001–2019: 66,699 ha). Contrary to this, 5 focus sites show spatio-temporal variability in their annual RTS dynamics, with alternating periods of increased and decreased RTS development, indicating a close relationship to thaw drivers. The majority of identified RTS was active from 2000 onward and only a small proportion initiated during the assessment period, indicating that the increase in RTS-affected area was mainly caused by enlarging existing RTS and not by new RTS. The detected increase in RTS dynamics suggests advancing permafrost thaw and underlines the importance of assessing abrupt permafrost disturbances with high spatial and temporal resolution at large-scales. Obtaining such consistent disturbance products will help to parametrise regional and global climate change models.

1. Introduction

Permafrost is warming globally and experiences intensifying rates of degradation (Biskaborn et al., 2019; Vasiliev et al., 2020; Farquharson et al., 2019). As permafrost is defined by the thermal state of the ground, with a temperature at or below 0 °C degrees for at least two consecutive years, the state and extent of permafrost is highly dependent on the prevailing thermal regime of the land surface (Brown et al., 1997). Key indicators of Arctic climate change such as increasing air temperatures, intensifying precipitation events, declining sea ice thickness and spring snow cover extent impact the state of permafrost (Box et al., 2019), ultimately leading to increased permafrost temperatures and inducing widespread permafrost thaw (Biskaborn et al., 2019). Near-surface permafrost loss impacts whole landscapes (Jorgenson and Grosse, 2016), ecosystems (Schuur and Mack, 2018), hydrological systems (Liljedahl et al., 2016), urban infrastructure (Hjort et al., 2018) and soil carbon accumulation and decomposition (Hicks Pries et al., 2015; Walter Anthony et al., 2018), resulting in increased rates of soil organic

---

* Corresponding author at: Alfred Wegener Institute Helmholtz Centre for Polar and Marine Research, Telegrafenberg A45, 14473 Potsdam, Germany.
E-mail address: alexandra.runge@awi.de (A. Runge).

https://doi.org/10.1016/j.rse.2021.112752
Received 19 March 2021; Received in revised form 7 October 2021; Accepted 11 October 2021

carbon release (Schuur and Abbott, 2011; Turetsky et al., 2019).

Remote sensing cannot directly observe permafrost as it is a subsurface phenomenon defined by ground temperature only, but it can give estimations on the distribution, magnitude and impact of permafrost thaw by detecting landforms and processes associated with melt of excess ground ice. Given the remoteness and vast extent of permafrost regions (about $21 \times 10^6 km^2$ (Obu et al., 2019)), remote sensing-based data and techniques are the only tools to detect, monitor and assess permafrost disturbances at regional to continental scales covering diverse and heterogeneous permafrost landscapes with spatial and temporal consistency. Open image archives and newly available cloud-computing possibilities led to an expanded development of remote sensing-based time series and disturbance detection algorithms (Zhu, 2017). Especially the Landsat archive, containing the longest continuous data set comprising nearly 50 years of multi-spectral high resolution (30 m) images acquired with a 16-day revisit cycle, has been used for large-scale time series assessments (Wulder et al., 2019). Prominent examples are the annual global forest maps (Hansen et al., 2013) and global surface water changes (Pekel et al., 2016). Advanced disturbance algorithms differ in targeted observed change (gradual vs. abrupt), temporal input data frequency, and whether they detect past changes or conduct near real-time monitoring (Zhu, 2017). The existing algorithms provide diverse assessment options. However, change and disturbance detection in northern high latitudes are still challenging as time series studies with optical remote sensing are restricted due to frequent cloud cover, short summer periods, and low illumination angles. This confines data availability drastically and limits algorithm applications that require high temporal input data. Yet, the combination of imagery from similar sensors, such as Landsat and Sentinel-2, increases data availability in the northern high latitudes strongly and permits change and disturbance detection at high temporal resolution (Runge and Grosse, 2019, 2020).

Permafrost warming is observed to cause widespread gradual active layer deepening across the pan-arctic permafrost region (Park et al., 2016). Ice-rich permafrost is particularly vulnerable to rapid thaw and erosion as high ground ice contents may accelerate degradation by thermokarst (Kokelj and Jorgenson, 2013) and thermo-erosion processes (Are, 1988). These processes are often driven by disturbances such as strong warming or precipitation events, hydrological changes, fires, or direct anthropogenic impacts on the soil thermal regime (Grosse et al., 2011). Resulting degradational landforms include thermo-erosional gullies and valleys (Morgenstern et al., 2021), degrading ice wedge polygons (Liljedahl et al., 2016), thermokarst lakes (Grosse et al., 2013), steep permafrost coastal bluff erosion (Günther et al., 2013), active layer detachment slides (Lewkowicz, 2007), and retrogressive thaw slumps (Burn and Lewkowicz, 1990), all which change and impact landscapes more drastically and much faster than gradual top-down thaw by active layer deepening (Turetsky et al., 2020). Despite this, large-scale assessments at high temporal resolution are still lacking for abrupt permafrost disturbances although understanding abrupt thaw is of high concern (Turetsky et al., 2019).

In this study we focus on the development of a remote sensing method to automatically identify and map retrogressive thaw slumps (RTS) across large-scale regions. RTS are abrupt permafrost disturbances that result from slope failure after thawing of ice-rich permafrost which is found either in ice-rich Yedoma regions (Strauss et al., 2017) or formerly glaciated areas that still contain permafrost-preserved buried glacial ice (Kokelj et al., 2017). Initiated by fluvial processes, thermo-erosion or mass wasting following heavy precipitation events and the exposure of ice-rich permafrost, RTS expand successively into the landscape with retrogressive growth of a steep headwall and the increase of a slump floor, rapidly and irreversibly changing the landscape (Ardelean et al., 2020; Kokelj and Jorgenson, 2013; Séjourné et al., 2015). RTS vary in size, ranging from under 0.15 ha to mega slumps of 52 ha and more (Ramage et al., 2017; Kokelj et al., 2015; Lacelle et al., 2015; Günther et al., 2015). Individual RTS are local, small-scale disturbances but often occur in regional clusters that then impact the surrounding landscape drastically by affecting topographic gradients and sediment transport (Kokelj et al., 2013; Mu et al., 2020), water quality (Kokelj et al., 2005), coastal erosion (Lantuit and Pollard, 2008; Ramage et al., 2017) and carbon cycling (Cassidy et al., 2017; Turetsky et al., 2020). Commonly observed RTS growth rates range from meters to tens of meters per year (Kokelj and Jorgenson, 2013). Increasing permafrost thaw due to climate change is predicted to intensify their thaw dynamics (Lantuit and Pollard, 2008; Segal et al., 2016; Lantz and Kokelj, 2008). Their combined impact on landscapes and biogeochemical cycling and the abruptness of their rapid development make RTS a highly important permafrost disturbance feature that require better monitoring and prediction capabilities.

Several local remote sensing studies found an acceleration of RTS dynamics by increasing numbers of active RTS, increasing sizes of RTS, and faster headwall retreat rates (Lewkowicz and Way, 2019; Ramage et al., 2017; Ward Jones et al., 2019), developments indicating intensified permafrost thaw and landscape degradation. Previous RTS studies covered a range of local to regional spatial extents and annual to decadal temporal resolutions. Commonly, RTS dynamics were estimated using very high resolution remote sensing imagery for limited local spatial extents from a selected number of points in time, restricted by availability of very high resolution imagery, allowing assessment of individual or a cluster of few RTS (Ardelean et al., 2020; Balser et al., 2014; Lantuit and Pollard, 2005, 2008; Lantz and Kokelj, 2008; Luo et al., 2019; Segal et al., 2016; Séjourné et al., 2015; Mu et al., 2020). Based on manually digitised RTS extents and limited fieldwork, these studies found increasing rates of RTS activity for varying time periods. Manual mapping using high resolution SPOT imagery provided a first regional insight into RTS distribution across a $1.27 \times 10^6 km^2$ region in NW Canada (Kokelj et al., 2017). Advancing these approaches, RTS disturbance trends were derived from multi-decadal Landsat image stacks, which helped mapping the distribution of active RTS at regional scales (Brooker et al., 2014; Kokelj et al., 2015; Nitze et al., 2018) or by applying a deep learning algorithm to map RTS from very high-resolution images in the Tibetan Plateau (Huang et al., 2020). These first automated mapping approaches enabled assessments of RTS dynamics at larger scales and results suggest that local permafrost disturbances occurring in regional clusters may have a significant impact on the landscape-scale. Ward Jones et al. (2019) and Lewkowicz and Way (2019) conducted the first high temporal resolution RTS assessments from annual input data. Their results indicate the increase in occurrence and thaw dynamics of RTS at high temporal resolution from manual RTS digitisation and image assessments and linked these to climatic drivers. Despite this, it still remains unknown how high temporal RTS dynamics are caused and may shift with climate change at a larger scale, as both studies are restricted to local study sites in the High Arctic. To achieve a better understanding of RTS temporal dynamics and their potential contribution to the global carbon cycle, more representative, large-scale, high temporal RTS assessments are necessary.

The aim of this study is to combine two key elements from the previous RTS assessments: firstly, to apply an automated RTS mapping approach for large-scale assessments, taking into account the diversity of permafrost regions; secondly, to conduct a high temporal resolution assessment, which captures the year-to-year dynamics of RTS. Our main objective is to assess RTS disturbance dynamics at high temporal resolution in North Siberia. For this, we developed an adaptation of LandTrendr, an algorithm for automated time series disturbance mapping and analysis (Kennedy et al., 2010), and designed a tailored algorithm parametrisation specifically for the assessment of RTS. The algorithm captures abrupt disturbances from annual Landsat mosaics, enabling the quantification and assessment of annual change. An annual resolution of data is appropriate to detect RTS dynamics related to annual thaw cycles and the 30 m spatial resolution is also sufficient to map RTS (Brooker et al., 2014; Nitze et al., 2018). However, for an enhanced spatial and temporal coverage at northern high latitude coastal areas we combine

Landsat + Sentinel-2 mosaics as input data for LandTrendr, overcoming some of the restrictions of optical remote sensing due to frequent cloud cover in Arctic regions (Runge and Grosse, 2020). We assess the applicability and accuracy of our method at local focus sites and derive quantitative annual disturbance dynamics of RTS from 2000 to 2019. Further, we upscale this method to an approximate $8.1 \times 10^6 km^2$ study region to map the occurrence and distribution of RTS and determine their annual disturbance dynamics for North Siberia.

2. Study area and methods

2.1. Study area

The study area covers the terrestrial northern high latitudes of Siberia, Russia, ranging from Taymyr Peninsula in the West (80° E) to Chukotka in the East (170° W) and roughly from 77° N to 55° N, comprising an area of approximately $8.1 \times 10^6 km^2$, here referred to as North Siberia. The majority of this area is characterised by continuous permafrost, discontinuous permafrost is found only in Chukotka as well as along the southern margins of the study area, where permafrost extent further declines to a sporadic or isolated coverage (Fig. 1). Unglaciated areas experienced long-term syngenetic freezing and continuous sedimentation during the Pleistocene, which led to the accumulation of ice-rich periglacial deposits (Kanevskiy et al., 2011). Ground ice volume varies across North Siberia but can reach more than 40% as in the southern part of the Lena Delta or even up to 80% in the Yedoma ice complex (Stolbovoi and McCallum, 2002; Strauss et al., 2017). The climate regions are broadly defined by the Arctic and Boreal zones and varying maritime and continental influences, resulting in a range of sub-regional climatic characteristics (Sayre et al., 2020). Bioclimatic zones in the region range from polar desert to tundra and taiga (Olson et al., 2001). Furthermore, the study area is defined by interior and coastal lowlands and several mountain ranges such as the Central Siberian Plateau, Verkhoyansk and Cherskiy, as well as major river systems such as the Lena, Yana, and Kolyma (Fig. 1).

Nine focus sites are used for the methodological set-up, especially calibration and validation, but also for in-depth result analysis. The focus sites cover the extent of the study area and represent varying geologic, geomorphologic, climatic and vegetational conditions, as specified in Table 1. Therefore, the selected focus sites cover a wide variability of ecosystems and represent the heterogeneous landscapes of North Siberia (Ali, 2020).

2.2. Ground truth data

LandTrendr was originally developed and designed to detect and capture forest disturbances. Therefore, we parametrised the algorithm to be applicable for RTS disturbance dynamics, comprising several individual steps, which required continuous calibration and validation. Ground truth (GT) data is sparse in North Siberia and only few RTS clusters are known so far. Therefore we concentrated on these as focus sites and collected as much GT data as available for calibration and validation. To achieve robust results we assessed every parametrisation step individually. Fig. 2 shows the general workflow to adapt LandTrendr to LT-LS2 (LandTrendr Landsat + Sentinel-2) and to parametrise LT-LS2 to be applicable to RTS.

We collected GT data for six focus sites across North Siberia to assess the temporal dynamics of RTS. We obtained very high-resolution (VHR) multi-spectral RapidEye images (5 m spatial resolution) (Krischke et al., 2000) as well as PlanetScope images (3 m spatial resolution) (Planet Team, 2017) for as many years as available for the focus sites (Table 2). There are only images available from 2013 onward, which implies that the period 1999–2012 cannot be assessed with RapidEye, PlanetScope or other data from other missions such as SPOT, Pléiades, WorldView or

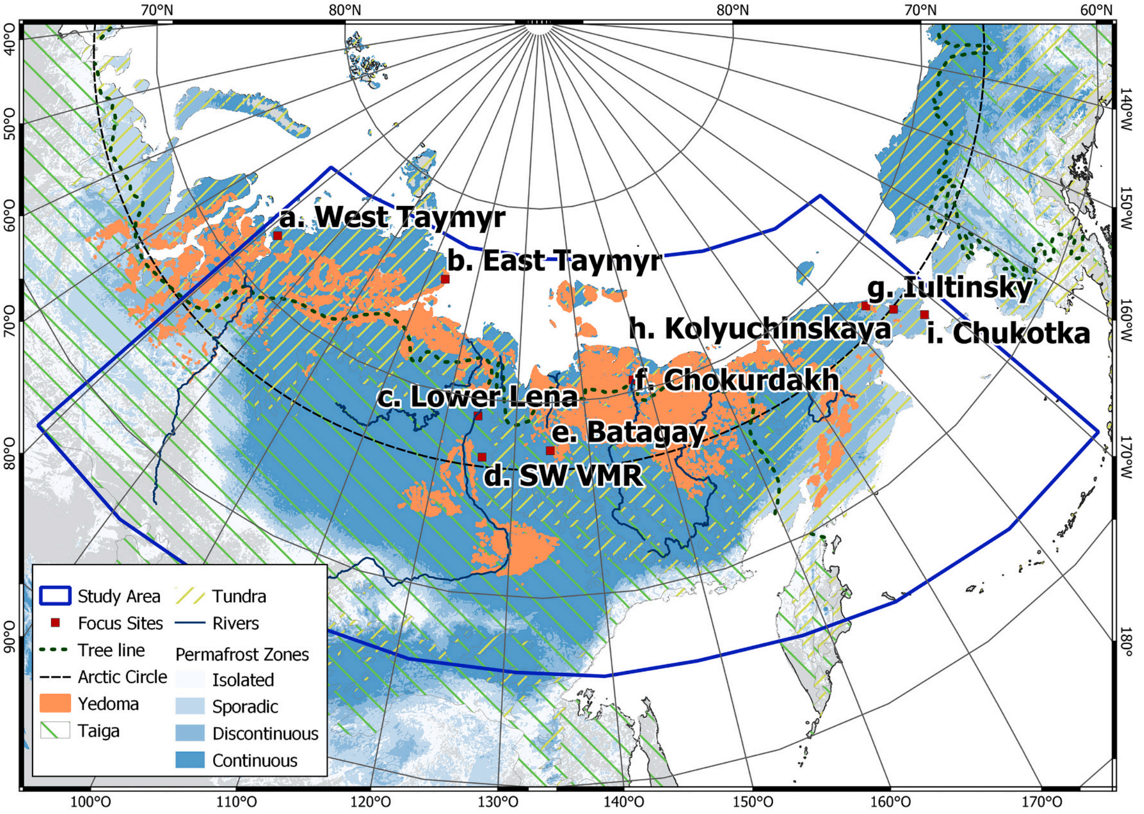

Fig. 1. Overview of the study area and focus sites across North Siberia. From West to East: a. West Taymyr, b. East Taymyr, c. Lower Lena, d. Southwest Verkhoyansk Mountain Range, e. Batagay, f. Chokurdakh, g. Iultinsky, h. Kolyuchinskaya, and i. Chukotka. Permafrost zones according to Obu et al. (2019), Yedoma extent according to Strauss et al. (2016) ecosystem according to Olson et al. (2001) and rivers from Natural Earth Data (Kelso and Patterson, 2010).

Table 1
Focus site locations and their characteristics. Mean annual air temperature (MAAT) and mean annual total precipitation (MATP) are derived from ERA5 reanalysis data based on a 30km-grid (C3S, 2017).

Focus site	Coordinates (centre)	Site characteristics	MAAT (2m) Jan /Jul [°C]	MATP [mm]
Lower Lena	69.1° N, 124.5° E	inland, hilly-mountainous, Yedoma, Taiga	-36.5 / 14.9	32
Iultinsky	67.7° N, 176.5° W	coastal, lowland, Tundra	-25.1 / 7.1	40
Chukotka	65.1° N, 172.1° W	coastal, lowland, Tundra	-19.9 / 9.0	52
East Taymyr	75.6° N, 113.6° E	coastal, lowland, Yedoma, Tundra	-28.6 / 3.8	28
West Taymyr	73.3° N, 86.9° E	coastal, hilly, Tundra	-27.1 / 8.1	43
Kolyuchinskaya Bay	66.7° N, 174.4° W	coastal, lowland, Tundra	-21.5 / 5.2	48
Chokurdakh	70.6° N, 147.9° E	coastal, lowland to hilly, Yedoma, Tundra	-33.9 / 10.2	24
Batagay	67.6° N, 134.8° E	inland, hilly to mountainous, Yedoma, Taiga	-41.9 / 15.7	21
Southwest Verkhoyansk Mountain Range	67.1° N, 125.6° E	inland, lowland, Yedoma, Taiga	-36.2 / 14.9	49

GeoEye. This lack of VHR data is a general limitation for North Siberia and unfortunately reflects how infrequent qualitatively sufficient VHR data is available. We manually digitised multi-temporal RTS extents from the VHR images by visualising false-colour composites for better RTS identification and with additional guidance of the permafrost region disturbance trend product (PRD) of the ESA GlobPermafrost project (Nitze et al., 2018) and ESRI's VHR satellite basemap (ESRI, 2017). The PRD is a Landsat-based multi-spectral trend product, indicated changes in the landscape. The collection of RTS extents shows the RTS size at different times and depicts the RTS development over several years at the six focus sites. Following the development of RTS as indicated by the digitised extents, we defined observation points along central transects through individual RTS, which are representative for different disturbance years of the slump (Fig. A.9) (Brooker et al., 2014).

Additionally, we used TimeSync for calibration and validation of the run parameters for the temporal segmentation of LT-LS2 (Cohen et al., 2010) with yearly Landsat+Sentinel-2 mosaics as input (Runge and Grosse, 2020). For every transect point (Fig. A.9) we assessed TimeSync's annual image chips and spectral trajectory to visually identify the timing of RTS disturbance, greatest disturbance segment, and the temporal segmentation of the overall spectral trajectory. As output of the manual TimeSync assessment, we recorded the year of disturbance (GT YOD) for every observation point (Table 2).

Lastly, we conducted a binary machine-learning classification to further remove abundant false positive objects. Based on the LT-LS2 disturbance detection results, we created a training and validation data set, by manually labelling all identified objects into either RTS (id 1) or no RTS (id 0) for five focus sites. For identification of the disturbance objects, we used again the PRD and ESRI's VHR stellite basemap (Nitze et al., 2018; ESRI, 2017). Table 3 gives an overview of the identified RTS for validation for each focus site. As described in Section 2.1 and Table 1 these focus sites cover heterogeneous landscapes in North Siberia as well as different types of RTS that are expected to occur (Table 3) and are therefore as representative as possible from the limited available data for ground truthing. Despite this, a level of uncertainty remains whether the full scope of RTS and their dynamics can be depicted for such a remote and large study area by the focus sites.

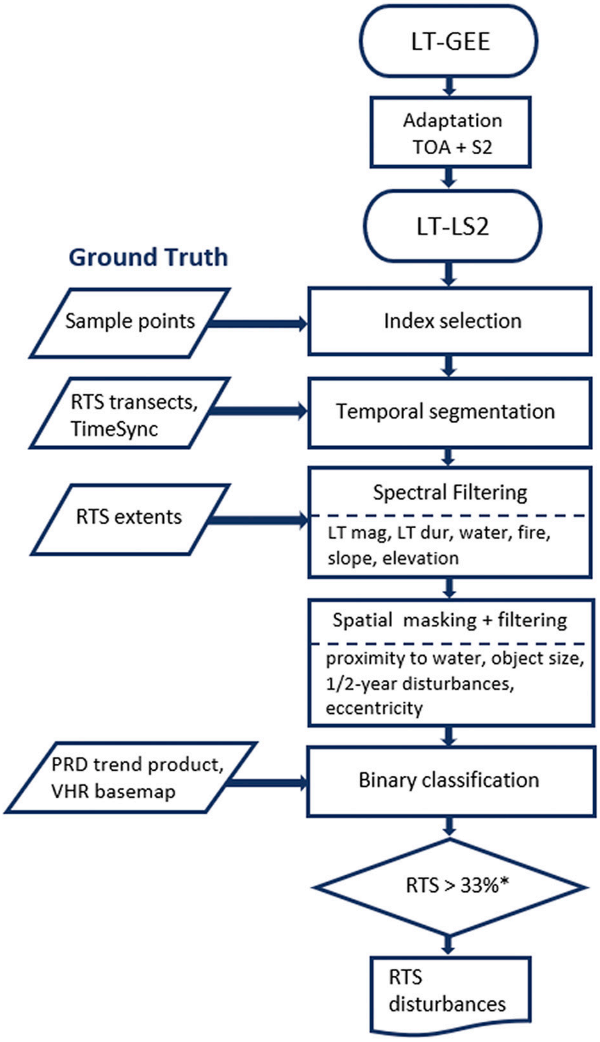

Fig. 2. Workflow to adapt LT-GEE to LT-LS2 and parametrise the algorithm for retrogressive thaw slump (RTS) assessment. * RTS probability score = 0.33% is the optimum threshold for an equilibrium between precision and recall in the classification as determined in Section 2.8.

2.3. Data and LandTrendr

Landsat and Sentinel-2 images are the input for this time series assessment as they together have the densest and longest continuous multi-spectral high resolution image archive. Their combined increased image acquisition frequency ensures good data coverage in northern high latitudes despite frequent cloud cover (Li and Roy, 2017), which is required for high-temporal time series analysis. In this assessment we adapted and applied the LandTrendr (Landsat-based detection of Trends in Disturbance and Recovery) algorithm (Kennedy et al., 2010). LandTrendr captures disturbance dynamics at high temporal resolution while only requiring annual mosaics as input, which is attainable in northern high latitudes by combining Landsat and Sentinel-2 (Runge and Grosse, 2020). LandTrendr is a time series segmentation algorithm that determines disturbance events and change trends from spectral trajectories on a pixel-basis. The sementation of spectral temporal trajectories consists of a sequence of break-points and straight segments which describe the temporal spectral trajectories more simplistically and eliminates noise from the time series (Fig. 3) (Kennedy et al., 2010). The temporal segmentation process is controlled by a set of run parameters which constrain the algorithm to achieve the best fitted temporal trajectory representation of the disturbance. Furthermore, the captured spectral

Table 2
Ground truth data at the focus sites from very high-resolution image data used for calibration and validation of the temporal segmentation and the spatial mapping step for LT-LS2 parametrisation. R = RapidEye, P = PlanetScope.

Site	Temporal segmentation	Years VHR images (R)	RTS transects	Observation points	Spatial mapping	Year RTS extent (R/P)
Chukotka	Calibration	2013, 2014, 2016, 2017, 2018, 2019	4	18	Calibration	2019 (R)
Batagay	Calibration	2013, 2016, 2017	4	19	Validation	2018 (P)
Lower Lena	Calibration	2013, 2014, 2016, 2018	4	24	Calibration	2019 (P)
Iultinsky	Validation	2014, 2016, 2018	3	20	Calibration	2018 (R)
Kolyuchinskaya Bay	Validation	2013, 2014, 2015, 2016, 2017, 2018, 2019	4	25	Validation	2019 (R)
Southwest VMR					Validation	2019 (P)

Table 3
The identified RTS in the disturbance data set for training of the machine-learning algorithm.

Study Site	RTS/Site characteristics	Number of RTS
Chukotka Coast	coastal RTS, discontinuous permafrost	53
Iultinsky	lakeshore RTS, 2-3 RTS per lake	66
Lower Lena	lakeshore RTS, 2-3 RTS per lake, LGM glacial ice extent	71
West Taymyr	lakeshore RTS, >3 RTS per lake, pre-glacial moraine deposits	116
Chokurdakh	lakeshore RTS, >3 RTS per lake, Yedoma	206
Total		**512**

change by the temporal segmentation can further be limited to a specific disturbance type and source by spectrally filtering the LandTrendr temporal segmentation results. LandTrendr is fully integrated on Google Earth Engine (GEE) as LT-GEE (Kennedy et al., 2018) and we followed the established workflow for adaptation (Fig. 2).

We relied on the full archives of Landsat (Thematic Mapper (TM), Enhanced Thematic Mapper Plus (ETM+) and Operational Land Imager (OLI)) and Sentinel-2 (MultiSpectral Instrument (MSI)) top-of-atmosphere (TOA) image collections for North Siberia from 1999 to 2020 and used images from the peak-growing season months, July-August. This reduces seasonal variations in reflectance values and ensures spectral comparability of land covers between years independent of phenological phases. An initial cloud cover filter of less than 80% was included as a first image quality criterion. We masked cloud and cloud shadow pixels based on the pre-processed metadata information for both image products (Landsat band: BQA (CFMASK), Sentinel-2 band: QA60 (adapted CFMASK)) to ensure data quality. Lastly, we applied spectral band transformations from MSI to OLI (Runge and Grosse, 2019) and OLI to ETM+ data (Roy et al., 2016) for spectral harmonisation and temporal continuity across the different sensors in the time series. The filtered, masked and harmonised image collections were input for a combined annual mosaicking process. We applied the medoid mosaicking function (Flood, 2013), which produces cloud-free, good quality and seasonally representative annual mosaics in Arctic-Boreal regions (Runge and Grosse, 2020). With these consistent annual mosaics we ensured temporal continuity in the time series and therefore had robust input for the LT-LS2 assessment.

2.4. Index selection

RTS can be mapped from multi-spectral data as there are distinct spectral differences between the RTS slump floor dominated by bare or sparsely vegetated, disturbed soils and wet mudflows and the surrounding undisturbed vegetated landscape (either tundra or forest) (Fig. 3). To determine the multi-spectral index, which captures the spectral change in the time series most reliably, we conducted a comparative analysis of six indices: the normalized difference vegetation index (NDVI) (Rouse et al., 1974), normalized burn ratio (NBR) (Key and Benson, 2005), normalized difference moisture index (NDMI) (Wilson and Sader, 2002), and the tasseled cap transformation indices greenness (TCG), brightness (TCB), and wetness (TCW) (Huang et al., 2002). At three focus sites, Lower Lena, Batagay and Iultinsky, we assessed the sensitivity of the indices to distinguish between pre-disturbance, RTS disturbance and post-disturbance in a time series (Quintero et al., 2019; Yang et al., 2018). The TCG and NDVI showed the clearest differentiation between the three stages in a spectral time series (Fig. 4). TCG showed more significant differences between pre-, post- and the RTS disturbance year compared to more subtle variation in NDVI. We therefore proceeded with TCG as the assessment index, which is also in accordance with Brooker et al. (2014).

2.5. LT-LS2 temporal segmentation

To identify the most suitable run parameters for RTS disturbances we defined the range of possible values for each parameter based on recommendations defined by the algorithm developers and previous adaptations (Table 4) and compared the different temporal segmentation outputs to the GT data (Section 2.2). In total we ran 48 LT-LS2 temporal segmentations for each calibration site and extracted the year of disturbance (LT-LS2 YOD) for the greatest loss segment for each transect observation point (Table 2). We calculated the error matrix between the GT YOD and LT-LS2 YOD for all temporal segmentation runs at each focus site and recorded the overall accuracy and Pearson's correlation coefficient to determine the best fitting temporal segmentation run and its corresponding run parameters. The segmentation results with the highest Pearson's correlation coefficient and overall accuracy were not the same for each focus site but showed tendencies for individual parameters. We therefore compared the runs with the highest scores and picked the run parameters with the highest agreement between sites and run options (Table 4). The selection of run parameters are in agreement with recommendations from Kennedy et al. (2010) and their sensitivity assessment for a successful LandTrendr set-up. With this parametrisation we ran LT-LS2 for the full study area of North Siberia and generated LT-LS2 change images for the greatest change segment. Six bands describe the disturbance at every pixel: 1) magnitude of spectral change, 2) year of disturbance, 3) duration of disturbance, 4) pre-change spectral value, 5) rate of spectral change, and 6) DSNR as a fit metric.

2.6. LT-LS2 spectral filtering

The majority of spectral change captured by LT-LS2 in the temporal segmentation is not RTS disturbance but due to general spectral change and trend, other landscape disturbances such as wildfires or lake drainage, erroneous pixels (cloud, haze, fire smoke) or other artefacts. To remove spectral change not associated to RTS disturbances, we filtered the temporal segmentation result by applying thresholds to the LT-LS2 image bands. We determined filter thresholds for magnitude of spectral change (mag) and duration in years (dur) that still map RTS but remove other spectral change. Spectral filtering disturbance mapping resultsfrom a range of possible threshold values (mag: 200, 400, 600,

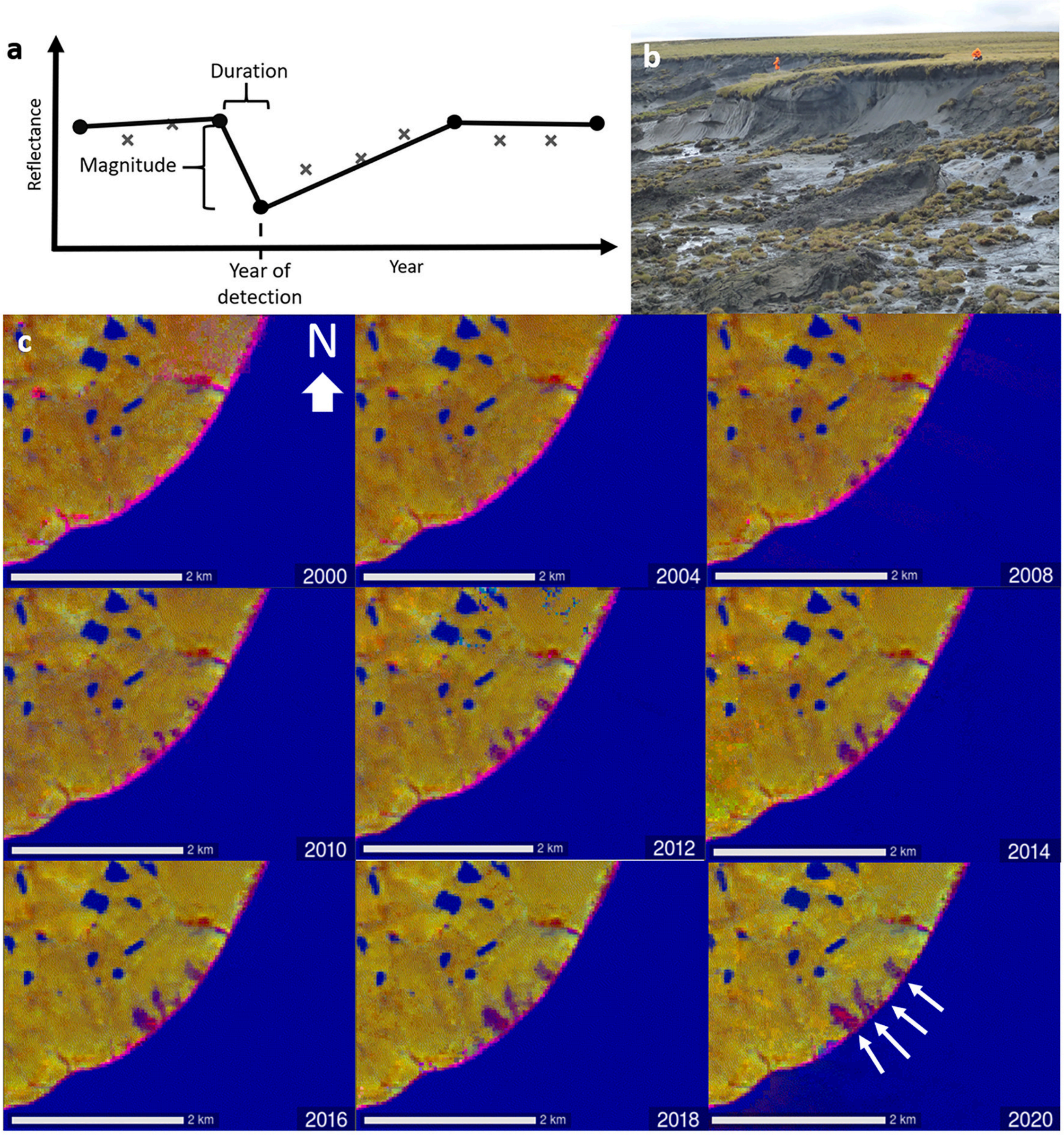

Fig. 3. Retrogressive thaw slump detection by LandTrendr. a. LandTrendr temporal segmentation schematic, indicating the year of detected disturbance from change in spectral magnitude and disturbance duration. b. Picture of coastal thaw slumping at Bykovsky Peninsula (129.2° E, 71.5° N) in 2014 (G. Grosse). Note persons for scale. c. Thumbnails indicating the development of RTS (white arrows in 2020) at the coast of Chukotka (172.2° W, 64.6° N) 2000–2020. Illustration based on a TCB/TCG/TCW visualisation in the LT-GEE Time Series Animator App (Justin, 2020).

800; dur: 1, 2, 4) were compared to GT data (Section 2.2). We compared the mapped area size of RTS from the 36 spectral filtering options to the GT area size (RTS extents 2019) and chose the threshold combination, which showed the highest correlation to the GT based on the Pearsons' correlation coefficient. With the exception of Chukotka Coast and East Taymyr, the Pearsons' correlation coefficients show high agreement between a dur value of 2 and mag values of 400, 600, and 800 (Table 5). A dur threshold of 2 ensures the inclusion of disturbance events that last at least 2 years which can be expected for RTS. At the same time this threshold excludes short term spectral disturbances, which are most likely related to anomalies, such as longer or earlier snow cover, as well as pixel artefacts. The best fitting mag threshold varied across the focus sites but there is a high correlation with several mag values (Table 5). The mag threshold is critical to ensure full spatial coverage of the RTS objects. We therefore chose the lower mag threshold of 400. While this enhances the RTS object coverage it also leads to high commission errors, including more non-RTS disturbance pixels and noise which has to be removed in the following steps.

2.7. *Spatial masking and object filtering*

The LT-LS2 disturbance map after spectral filtering, despite its explicit parametrisation to RTS disturbances, does not only depict thaw slumping features but includes other, spectrally similar disturbances, such as wildfires, active layer detachment slides, changes in river water levels. To further narrow the LT-LS2 disturbance map to RTS, we applied several environmental spatial masks (Table 6).

Following this, we performed object-oriented spatial filters to further exclude false positive disturbances and to restrict the subsequent analysis to RTS disturbances (Table 7). We identified disturbance objects with scikit-image's connected component algorithm in a 2-connectivity neighbourhood (Van der Walt et al., 2014) and extracted for every labelled object feature properties. Based on the LT-LS2 year of disturbance band, we derived the minimum year and maximum year of

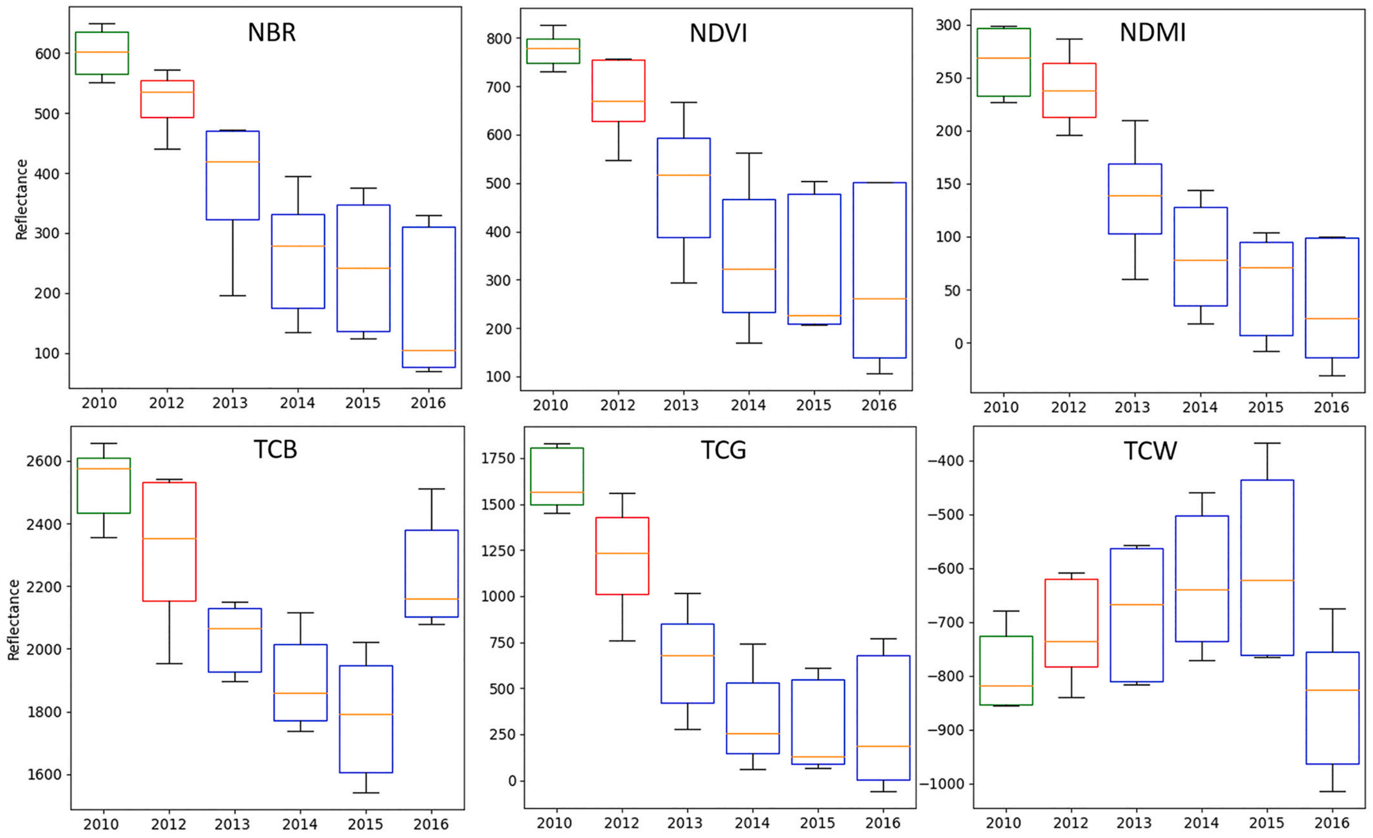

Fig. 4. Spectral indices for pre-disturbance (2010), disturbance (2012) and post-disturbance (2013–2016) years for the focus site Lower Lena. Boxplots illustrate the spectral reflectance dynamics from representative RTS disturbance pixels.

Table 4
List of necessary LT-LS2 run parameters for the temporal segmentation algorithm, indicating all tested values and eventually selected values (in bold and italic) for processing. Standard values were chosen for vertex count overshoot, minimum observations needed and one year recovery prevention. See Kennedy et al. (2010) for detailed parameter description.

Run parameter	Values
Max segments	3, ***4***, 6
Spike threshold	***0.75***, 0.9
Vertex count overshoot	3
Recovery threshold	***0.25***, 0.5
Best model proportion	***0.75***, 1.0
Pval	***0.05***, 0.1
Minimum observations needed	6
Prevent one year recovery	True

Table 5
The tested mag and dur values for spectral filtering with the highest Pearson's correlation coefficient for the calibration and validation focus sites.

Site	Magnitude	Duration	Pearson's correlation coefficient
Lower Lena	400	2	0.98
	600	2	0.92
Chukotka	800	2	0.51
	600	2	0.26
	400	2	0.24
Iultinsky	800	2	0.94
	600	2	0.70
	400	2	0.56
East Taymyr	200	2	0.37
	400	2	0.28
Southwest VMR	400	2	0.99
Kolyuchinskaya Bay	800	1	0.99
	600	2	0.97
	400	2	0.95

disturbance for every labelled object, representing the disturbance period of that object. The minimum mapping unit (mmu), maximum mapping unit (maxmu) (Lacelle et al., 2015; Lewkowicz and Way, 2019; Kokelj et al., 2015; Lantz and Kokelj, 2008; Segal et al., 2016; Ramage et al., 2017), object eccentricity, and disturbance period are used to differentiate between RTS, which evolve over multiple years and have a certain typical size, and other disturbances such as 2020 fire scars, remnants of previous fire scars or other extensive disturbances.

2.8. Machine-learning object filter

After spatial masking and filtering the disturbance data set still contained a high amount of commission errors (false positives). Therefore we applied a binary classification step to classify the disturbance object either as a RTS or other. The training and validation data set was introduced in Section 2.2 and Table 3. Based on the available GT RTS data only 13% (F1 score) of the identified disturbances were correctly identified RTS before the binary classification step (Table 9). Omission and commission scores cannot be assessed at this point, as only the disturbance objects identified up until the previous processing step were included for the five focus sites. There is no additional GT data available that could possibly specify missed RTS by our method. We used the pycaret (version 2.3) package in python to setup a classification pipeline. As input data we used basic statistics (min, mean, max values) of all LT-LS2 output bands, except "year of disturbance", and Landsat Tasseled Cap Index Trends (slopes of TC brightness, greenness and wetness) per polygon object. In the model comparison Light Gradient Boosting Machine (Ke et al., 2017) came out as the best model, where we used the F1

Table 6
Overview of spatial masks applied.

Mask	Data set	Threshold	Reference
Water	Global surface water data set		Pekel et al. (2016)
Fire	Global forest cover change		Hansen et al. (2013)
Slope	ArcticDEM	3–15 °	Porter et al. (2021)
Elevation	ArcticDEM	<250 m a.s.l.	Porter et al. (2021)
Water buffer	Global surface water data set	300 m buffer	Pekel et al. (2016)
Permafrost	Extent and Ground Temperature	Continuous, discontinuous	Obu et al. (2019)

Table 7
Overview of object-oriented spatial filters applied.

Filter	Threshold	Reference
Eccentricity	>0.75	empirically derived (Lower Lena, Chukotka, Iultinsky)
Minimum mapping unit (mmu)	0.36 ha	2*2 30 m pixels, Brooker et al. (2014)
Maximum mapping unit (maxmu)	15 ha	
Disturbance period	<2 years	unlikely RTS, but likely 2020 fires, remnant fire scars, ALDS, artefacts

score as the primary estimator metric. To deal with the extreme class imbalance we used the Synthetic Minority Oversampling Technique (SMOTE) resampling algorithm (Chawla et al., 2002), which is implemented in pycaret. Furthermore we calculated overall classification metrics Accuracy and Kappa as well as binary and class specific metrics area under curve (AUC), precision and recall. We optimised the model and performed a 10-fold stratified cross-validation on the input data set. We used pycaret's built-in model evaluation functionality to determine the best separation threshold between classes, as the initial discrimination was strongly imbalanced with a bias towards the no-slump class. We repeated the cross-validation on a regional basis, training on four tiles and validating on the fifth, rotating through all tiles. We added the regional validation to test the transferability to unseen regions. Finally, we trained the production model on all five ground-truth tiles and ran the inference on the entire study area. The output data set contains final class labels (0 or 1) and class specific probability scores. With this we reduced the false positives of LT-LS2 drastically, which improved the RTS disturbance mapping greatly compared to the purely LT-LS2 automated algorithm.

2.9. *Method accuracy*

2.9.1. *LT-LS2 temporal segmentation accuracy*

The results from the comparison between GT YOD and LT-LS2 YOD showed that the LT-LS2 temporal segmentation depicts the progression of annual temporal dynamics of RTS well. The Pearson's correlation coefficient between GT YOD and LT-LS2 YOD show an agreement of up to 0.98 for individual RTS transects (Chukotka 1 and 4, Iultinsky 2, 3 and Kolyuchinskaya Bay 1), which verifies that the LT-LS2 temporal segmentation parametrisation captures the progression of RTS thaw dynamics at an annual temporal resolution (Table 8). Individual transects show little agreement between the GT YOD and LT-LS2 YOD data (Lower Lena 1 and 2, Iultinsky 1, Kolyuchinskaya Bay 2 and 3). A visual assessment showed that this is mainly due to individual faulty data points in the temporal spectral trajectories, which resulted from irregularities in the mosaics, for example from ETM+ scan-line errors or from individual invalid pixels, which deviated from the expected temporal trajectory. Hence, overall LT-LS2 captures and depicts the dynamic development of RTS well. Further, we derived the mean deviation and standard deviation between absolute GT and LT-LS2 identified year of disturbance for the transect observation points to evaluate the precision of detected disturbance year (Table 8). The mean deviation ranges from -4.4 to +3 years for Kolyuchinskaya Bay transect 3 and Lower Lena transect 1, respectively. Half of the mean values demonstrate that LT-LS2 YOD values are later compared to the GT YOD, which shows a delay in disturbance recognition in the LT-LS2 analysis. Contrary to this, negative mean values illustrate that LT-LS2 implies a disturbance earlier than the GT YOD data set. An issue is probably that with a spatial resolution of 30 m we have to account for mixed pixels, which delay the detection of a disturbance, as the multi-spectral data only recognises the disturbance when bare soil dominates the mixed pixel. The assessment shows no clear trend on whether LT-LS2 identifies RTS disturbances rather too early or delayed but that we have to account for inaccuracies of approximately ±2 years for the disturbance year of LT-LS2.

2.9.2. *Machine-learning object filter accuracy*

The validation results prove the challenging task of mapping RTS at large-scale. 10-fold cross-validation (CV) on the full GT data set without regional differentiation revealed a mean accuracy (statistics of all 10 folds) of 0.9479±0.0106 and kappa of 0.5452±0.1042 (Table 9). The class specific performance for RTS (id 1) metrics revealed a mediocre performance with a F1 score of 0.609. The higher precision (0.655) compared to recall (0.569) shows a slight bias towards an "under-detection" of RTS. To overcome this bias and to receive a balanced classification we used the "threshold" estimator in pycaret. This

Table 9
Overall 10 fold cross-validation. Mean and standard deviation of scores from all 10 folds. *Accuracy assessment of the RTS training data set before the binary classification. AUC = Area Under the Curve.

	Accuracy	AUC	Recall	Precision	F1	Kappa
Mean*	0.07				0.13	
Mean	0.9479	0.9014	0.4846	0.6765	0.5622	0.5355
Standard Deviation	0.0106	0.0172	0.1025	0.1034	0.1013	0.1061

Table 8
Assessment of the LT-LS2 temporal segmentation based on the GT YOD and LT-LS2 YOD transect observation points. The first value is the Pearson's correlation coefficient indicating the general level of agreement between GT and LT-LS2. The second value is the mean deviation between the absolute GT YOD and LT-LS2 YOD value and the third the standard deviation, demonstrating the error in absolute year of disturbance in the temporal segmentation. For transects marked with an asterisk we excluded the earliest transect point for the mean and standard deviation.

Step	Site	All transects	Transect 1	Transect 2	Transect 3	Transect 4
Calibration	Chukotka Coast	0.63 / -0.3 / 2.6	0.65 / 1* / 1.4	0.40 / -1.3 / 2.8	0.98 / -2 / 2.1	0.95 / 2* / 1.2
	Batagay	0.78 / 0.8 / 3.3	0.8 / 1.7* / 0.9	0.66 / 2.8* / 1.9	0.81 / -2.8 / 3.4	0.76 / 2.5* / 1.2
	Lower Lena	0.23 / 0 / 3.9	0.22 / 3* / 5.1	0.14 / 1.5 / 1.4	0.81 / 1.8 / 0.7	0.59 / -1.7* / 4.6
Validation	Iultinsky	0.49 / -0.13 / 3.9	0.06 / -1.5* / 6.2	0.90 / 2.3* / 1.8	0.92 / -0.7 / 1.8	
	Kolyuchinskaya Bay	0.40 / -2.1 / 5.3	0.97 / -0.4 / 1.0	0.05 / -1.4* / 5.4	0.05 / -4.4 / 6.7	

revealed an optimum threshold (probability score for class 1) of 0.33 to maximize the F1 score and a threshold of 0.25 for an equilibrium of precision and recall (Fig. A.10). The regional cross-validation (five sites) revealed the challenges of model transferability. RTS class specific F1 score ranged from 0.07 (Lower Lena) to 0.37 (West Taymyr) and therefore lower than a CV on the entire data set (Table 10). The classification bias, as observed on the full CV, was more diverse in the regional CV. Three of five regions have a higher recall, while only two exhibit an excess in precision.

3. Results

3.1. Focus sites

For five focus sites we mapped RTS and assessed their annual thaw dynamics in detail to demonstrate the capability and applicability of our method. The focus sites comprise a square area of 625 km^2 and represent known RTS clusters, with varying RTS and densities (Table 11). Chukotka presents a coastal site with many active RTS along the coastline. Here, as the RTS grow retrogressively, neighbouring RTS merge together and form bigger RTS objects with time. At Iultinsky and Lower Lena we identified RTS at lake shores and often 2–3 RTS at one lake. Both focus sites are located at the border of the Last Glacial Maximum (LGM) glacial ice extent in Siberia and are close to areas with ice-rich Yedoma deposits (Fig. 7). The other two focus sites, West Taymyr and Chokurdakh, also feature RTS at lake shores but often with more than 3 RTS at a lake. Chokurdakh is special, as not only individual RTS developed but complete lake shores erode. Here, LT-LS2 often identified multiple individual RTS, for the more active erosion parts of the shore. Chokurdakh is characterised by extensive Yedoma deposits, whereas West Taymyr is located within pre-LGM glacial moraine complexes. The minimum RTS size with 0.45 ha was found at Iultinsky, Chukotka and Chokurdakh, the predefined mmu. The biggest identified RTS is in Chukotka with 14.94 ha, the maxmu. The mean RTS size for the sites ranges from 1.4 to 4.8 ha. In West Taymyr the average RTS activity duration is 11.8 years compared to 15.2 years in Chukotka. The initial RTS-affected area in 2000 per focus site varies greatly (Iultinsky: 5.9 ha, West Taymyr: 69 ha) and likewise does the increase in RTS-affected area from 2001 to 2019. The RTS-affected area in Iultinsky, West Taymyr and Lower Lena increased by 188%, 144% and 141%, respectively. In contrast, the area increase of 73% was much lower for Chokurdakh.

The first and last year of slump activity for each identified RTS and the summarised RTS-affected area per year, indicating the annual RTS growth, show the dynamic progression of RTS (Fig. 5) as visually depicted in Fig. 6. The first year in the assessment period, 2000, comprises not only newly disturbed RTS area in 2000 but also the accumulated dynamics from previous years before our time series starts (approximately 1997–2000) (Fig. 5). The annual RTS area analysis shows that the increase in RTS area is not uniformly during the observation period but that distinct years with accelerated RTS area growth can be determined. Iultinsky had two periods of increased slump activity, 2008–2010 and 2015–2018, with the highest RTS area growth in 2008 (Fig. 5d). Similarly, West Taymyr also showed two periods with increased slump activity, 2005–2006 and 2012–2017. The RTS-affected area in Lower Lena increased in 2008 and lasted until 2017, with the exception of 2014. About 60% of the RTS in West Taymyr showed their last activity in 2016–2017 (Fig. 5c), which is either the peak slump year (2016) or one year later (2017). This suggests that the accelerated slump activity was caused by a temporary trigger. There is little new RTS initiation during the assessment period in Iultinsky and Lower Lena alike and more than 80% of the identified RTS were active since 2000. Most of the RTS had their last activity in the second half of the time series, specifying higher slump activity during the last two decades in Iultinsky and Lower Lena compared to West Taymyr. Chokurdakh und Chukotka show very similar annual RTS-affected area trends as Iultinsky and Lower Lena. The results show an alternation between time periods of high RTS activity and less RTS development during the observation period (Fig. A.12).

Table 10
Regional Cross-validation (RTS class only).

Site	Precision	Recall	F1	Support (n objects)
Chukotka	0.45	0.27	0.34	48
Iultinsky	0.28	0.34	0.30	56
Lower Lena	0.04	0.44	0.07	61
Chokurdakh	0.38	0.18	0.24	212
West Taymyr	0.63	0.26	0.37	110

3.2. North Siberia

Within our study area of approximately 8.1×10^6 km^2 covering North Siberia, a total number of 50,895 RTS were identified and mapped. The majority of RTS was found between 61 to 73° N (Fig. 8b). This RTS abundance is highly related to the uneven latitudinal land mass distribution in the study area, with less land area north of 72° N reducing the number of RTS. Similarly to this, the lower latitudes in the East of the study area (140° E, 55–60° N) cover less land mass, which explains the lower geographic boundary of identified RTS. Fig. 7 shows the geographic density of identified RTS for $40km \times 40km$ grid cells. The majority of RTS were identified in the continuous permafrost zone, more than 70% of the RTS (Fig. A.11c). Where the permafrost extent becomes discontinuous, sporadic or isolated permafrost, RTS occurrence and density decrease as well. Furthermore, the RTS density map reveals clusters of RTS between 80 to 90° E in the West of the study area, between 140 to 160° E and north of 65° N and along the border of the LGM glacial ice extent in Siberia (Ehlers and Gibbard, 2003). The abundance of RTS along the margins of the LGM glaciation is most likely associated to degrading buried glacial ice in moraines (Barr and Clark, 2012; Kokelj et al., 2017). Moreover, the occurrence and density of RTS correlates closely with the distribution of thick ice-rich Yedoma permafrost deposits that are particularly vulnerable to thermokarst and thermo-erosion processes such as RTS (Fig. 7) (Strauss et al., 2017, 2016). About 14% of the RTS are within Yedoma deposits and almost 70% in close vicinity (<10km) (Fig. A.11d). A high density of RTS can be found in central Yakutia near Yakutsk, a known hot spot region for permafrost degradation and thermokarst development (Séjourné et al., 2015; Ulrich et al., 2017). In contrast to this, we also identified vast areas with no or low RTS densities across North Siberia, most notably in mountainous regions and the central West of the study area.

Assessing the mapped RTS in relation to elevation and slope showed, that the majority of RTS were found in a sloped terrain of 2–4 ° (about 30%) (Fig. A.11b). The occurrence of RTS decreased with increased elevation but is also cut-off by the elevation threshold of 250 m a.s.l (Fig. A.11a).

The normalised area frequency plot (Fig. 8d) illustrates that the vast majority of identified RTS are small and close to the predefined mmu. About 50% of all identified RTS are smaller than 1.17 ha and 90% of the RTS are smaller than 3.42 ha, which indicates that the normalised area frequency is positively skewed. The proportion of bigger slumps is much lower. The distribution is positively skewed because RTS are rather small-scale disturbance features, with commonly reported sizes of 0.4–5.3 ha (Lacelle et al., 2015; Segal et al., 2016), which our results show as well. RTS exceeding this size by far, so-called mega slumps, occur but are less common. Secondly, RTS are polycyclic which is another reason for the predominance of smaller identified RTS objects. RTS often alternate between periods of active degradation and periods of stabilised dormancy, which can differ spatially with only part of a stabilised RTS re-initiating, depending on slumping drivers and environmental factors such as remaining ice content, exposure of the ice, the sloped terrain, drainage and sediment transport, and climatological conditions (Balser et al., 2014; Kokelj et al., 2009). The stabilised part of

Table 11
Overview of identified RTS for the focus sites (625 km^2) and all of North Siberia. The number of identified RTS, average slump size and the average slump activity duration (last - first year of disturbance pixel) are based on the identified RTS objects. The summarised slump area for 2000 and the summarised slump area from 2001 to 2019 are compiled from all RTS pixels in a focus site. The summarised area from 2001 to 2019 percentage indicates the area growth compared to the RTS area in 2000. The peak growth years are the two years with the highest RTS area in the time series. *The initial RTS area was derived from 2000 to 2001.

Site	Number of RTS	RTS min/mean/max [ha]	Average slump activity duration [yr]	RTS area in 2000 [ha]	RTS area from 2001–2019 [ha]/[%]	Average growth/year [%]	Average growth/RTS [%]	Peak growth years ([ha])
Lower Lena	18	0.72 / 2.34 / 6.2	13.7	17.5	24.6 / 141	7.4	7.8	2013 (3.9), 2015 (3.7)
Iultinsky	9	0.45 / 1.9 / 8.46	11.9	5.9	11.16 / 188	9.9	20.9	2008 (2.61), 2009 (1.53)
Chukotka	9	0.45 / 4.83 / 14.94	15.2	19.5	23.9 / 123	6.5	13.6	2016 (5.4), 2007 (2.97)
Chokurdakh	64	0.45 / 1.4 / 7.56	12.3	50.9	36.9 / 73	3.8	1.1	2009 (6.03), 2011 (5.58)
West Taymyr	88	0.45 / 1.9 / 11.8	11.8	69.0*	99.5 / 144	7.6	1.6	2016 (43.2), 2013 (20.5)
North Siberia	50,895	0.45 / 1.7 / 14.94	12.3	20,158	66,699 / 331	17.4	0.007	2019 (9,669), 2016 (7,136)

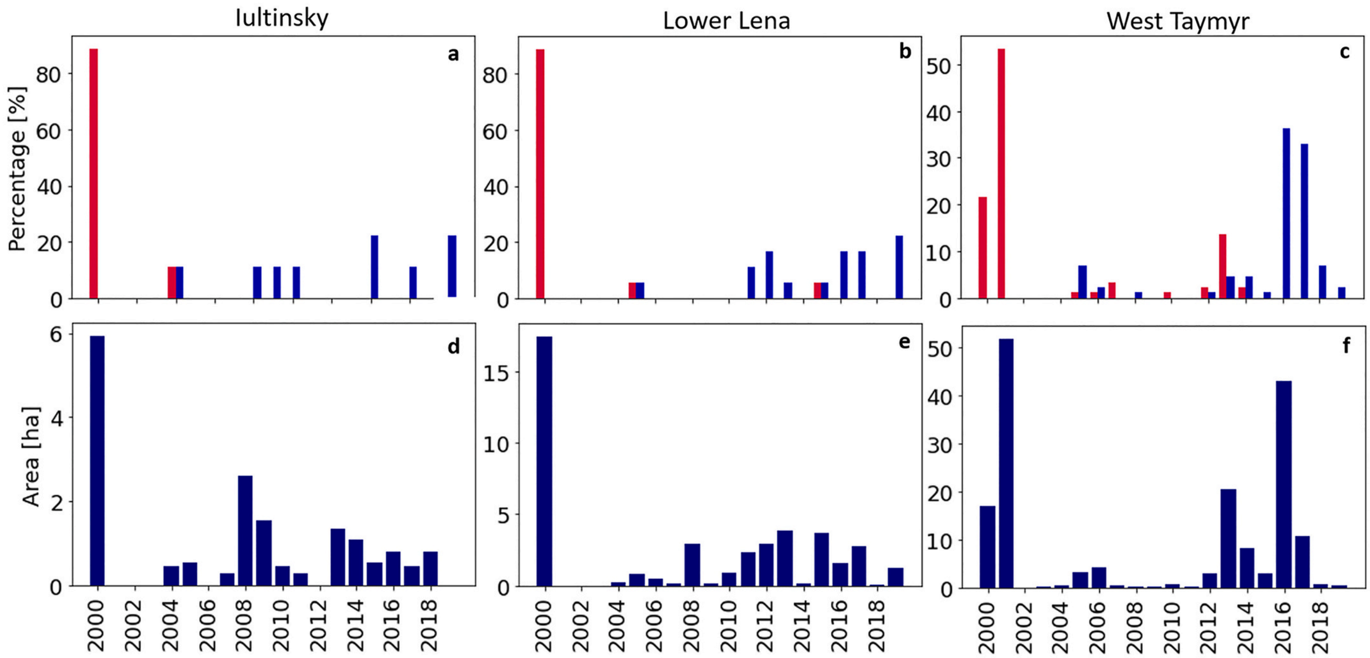

Fig. 5. The first year of RTS activity (red bar) and last year of RTS activity (blue bar) for Iultinsky, Lower Lena and West Taymyr on the top panel (a–c) and the annually summarised RTS areas for the same sites below (d–f).

a RTS cannot be detected by LT-LS2 as the temporal spectral signature of these areas does not resemble a disturbance trajectory. LT-LS2 only detects the actively degrading RTS areas, capturing only disturbances occurring within the assessment period (1999–2000), which might not represent the full RTS extent. Therefore, we consider our findings of RTS numbers and areas conservative low.

Most slumps had their first active year at the start of the assessment period with almost 50% and 25% in 2000 and 2001, respectively (Fig. 8a). The remaining RTS had their first activity year in the course of the time series until 2016 but no RTS initiations were detected in 2017–2018. About 25% of the RTS had their last slump activity in 2019, which is the end of the time series. However, a bigger proportion of about 30% of the RTS deceased slumping already before the end of the assessment period, namely in 2016–2018. The overall summarised RTS-affected area increases steadily during the time series, illustrating extended annual RTS growth and development (Fig. 8c). The years 2000 and 2001 show particularly high annual RTS areas. As these are the first years in the time series, we expect them to contain the accumulated disturbance history of recent years. Results for 2000 and 2001 are therefore strongly influenced by an accumulative effect of first detections at the time series beginning and thus are more difficult to interpret. Accordingly, the trend line was only calculated for data from 2002 to 2019 (Fig. 8c). Heightened increase rates were determined for 2016, 2017 and 2019. From 2001 to 2019 the RTS-affected area increased by 331% compared to 2000, which shows a drastic increase in area affected by permafrost degradation in only 19 years (Table 11).

Combining these results, we can determine, that the increase in RTS-affected area at the end of the time series is not caused by newly or re-initiated RTS but most likely by RTS growth of already existing and active RTS. Furthermore, the high number of inactive RTS in 2016–2018 (last year of activity), suggests that the increase in RTS area is not necessarily caused by successive thaw, which would prevail for a longer time period, but by explicit triggers in those years. Whether these RTS remain inactive and stabilise for a longer period cannot be derived from this assessment.

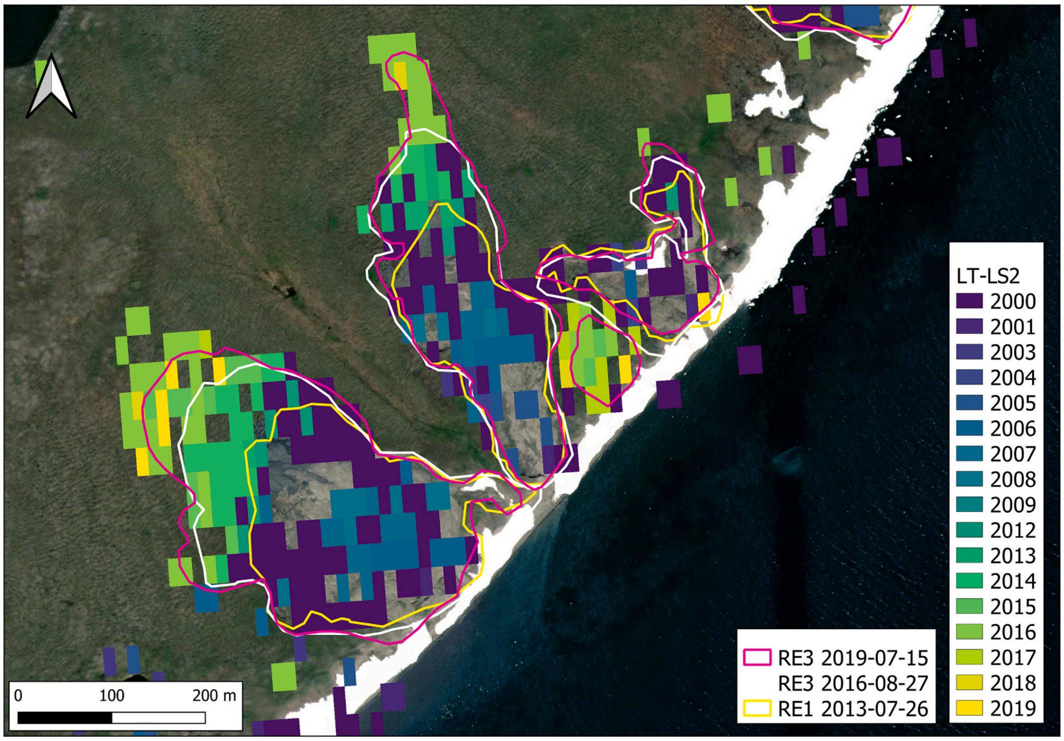

Fig. 6. Annual progression of RTS in Chukotka (172.2° W, 64.6° N), showing the year of disturbance for every pixel. Digitised yearly RTS extents from RapidEye images are indicated. RTS outline in pink from 2019, in white from 2016, and in yellow from 2013. Background is Esri Satellite Basemap (ESRI, 2017).

4. Discussion

4.1. Mapping of RTS

Our results are overall in agreement with previous studies. The mean size of identified RTS ranges between 1.4 ha (Chukordakh) to 4.8 ha (Chukotka), which slightly exceeds the RTS sizes recorded by previous studies stating average RTS sizes of 0.15–1.63 ha (Ramage et al., 2017; Lewkowicz and Way, 2019). The range of previously published mega slump sizes, 3.8–9.9 ha, as described by Kokelj et al. (2015) for NW Canada, is comparable with the maximum RTS sizes in our study of 6.2–11.8 ha (Chukotka even 14.94 ha). LT-LS2 might be biased towards larger features due to the lower resolution, whereas other studies use much higher resolution aerial and and satellite imagery to quantify average RTS size. But overall the agreement between studies indicates that LT-LS2 is well suited to identify RTS across very large regions.

Furthermore, we found a strong correlation between the detection of RTS and environmental factors. RTS generally occur in ice-rich permafrost areas, mostly from glaciogenic deposits or syngenetic permafrost, along sloped terrain and in proximity to lakes, rivers and coasts, where climatic conditions drive their development (Kokelj and Jorgenson, 2013; Kokelj et al., 2017; Ardelean et al., 2020). Our results also show that the majority of the RTS and the highest RTS density can be found in the proximity to the LGM glacial ice extent (moraine complexes) and in areas with thick ice-rich Yedoma deposits. This agrees with prior findings of increased RTS occurrence in such areas in local and regional studies from Canada (Ward Jones et al., 2019; Lewkowicz and Way, 2019; Lacelle et al., 2010) and Alaska (Balser et al., 2014), emphasising that very ice-rich permafrost is a determining factor for RTS. Additionally, the close fit between detected RTS and ice-rich permafrost in this study verifies that our applied automated method identifies RTS correctly. The RTS density distribution underlines the vulnerability of ice-rich permafrost to abrupt thaw and furthermore, the threat of rapidly mobilizing increased amounts of sediment and organic carbon over short periods of time (years) in icy permafrost regions experiencing thaw.

However, these RTS mapping results were constrained by the mmu and maxmu which we applied to obtain reliable results regarding the spatial resolution (30 m), temporal resolution (annual), GT data availability for this large-scale assessment and to avoid confusion with other land cover disturbances and changes such as fires or active layer detachment slides, which have shorter disturbance dynamic periods, as described in Section 2. Mapping RTS smaller than the mmu is not feasible at this spatial resolution as the volume of false positives would have been increased and the limited available GT data set would not be sufficient to mask or filter these in the post-processing steps. Applying a similar workflow to VHR data such as RapidEye or PlanetScope would improve identification and mapping of smaller RTS but we currently lack the temporal coverage of VHR data in the northern high latitudes (Table 2).

Additionally, the maxmu prevented to detect large RTS or mega slumps, such as Batagay (67° N, 134° E) which is the largest mapped RTS (>70 ha) in Northeast Siberia with a headwall retreat rate of up to 30 m per year (Günther et al., 2016). Since the ancillary data sets were not sufficient to differentiate reliably between large RTS and other bigger disturbances and land cover changes, as for example Hansen et al. (2013) forest change currently lacks fires from 2020, we opted to exclude larger disturbance patches due to heightened uncertainties. While this is a limitation, the amount of large RTS or mega slumps is much smaller compared to the average RTS (Kokelj et al., 2015) and should therefore not affect our results greatly as we capture the most relevant range of RTS sizes. Therefore, the method presented here is a compromise between mapping RTS reliably (constrained between mmu and maxmu) with an automated algorithm at large-scale and being able to validate the results with limited GT data. Hence, we consider our mapping results as conservatively low and expect an actually higher number of RTS in North Siberia than identified in this study.

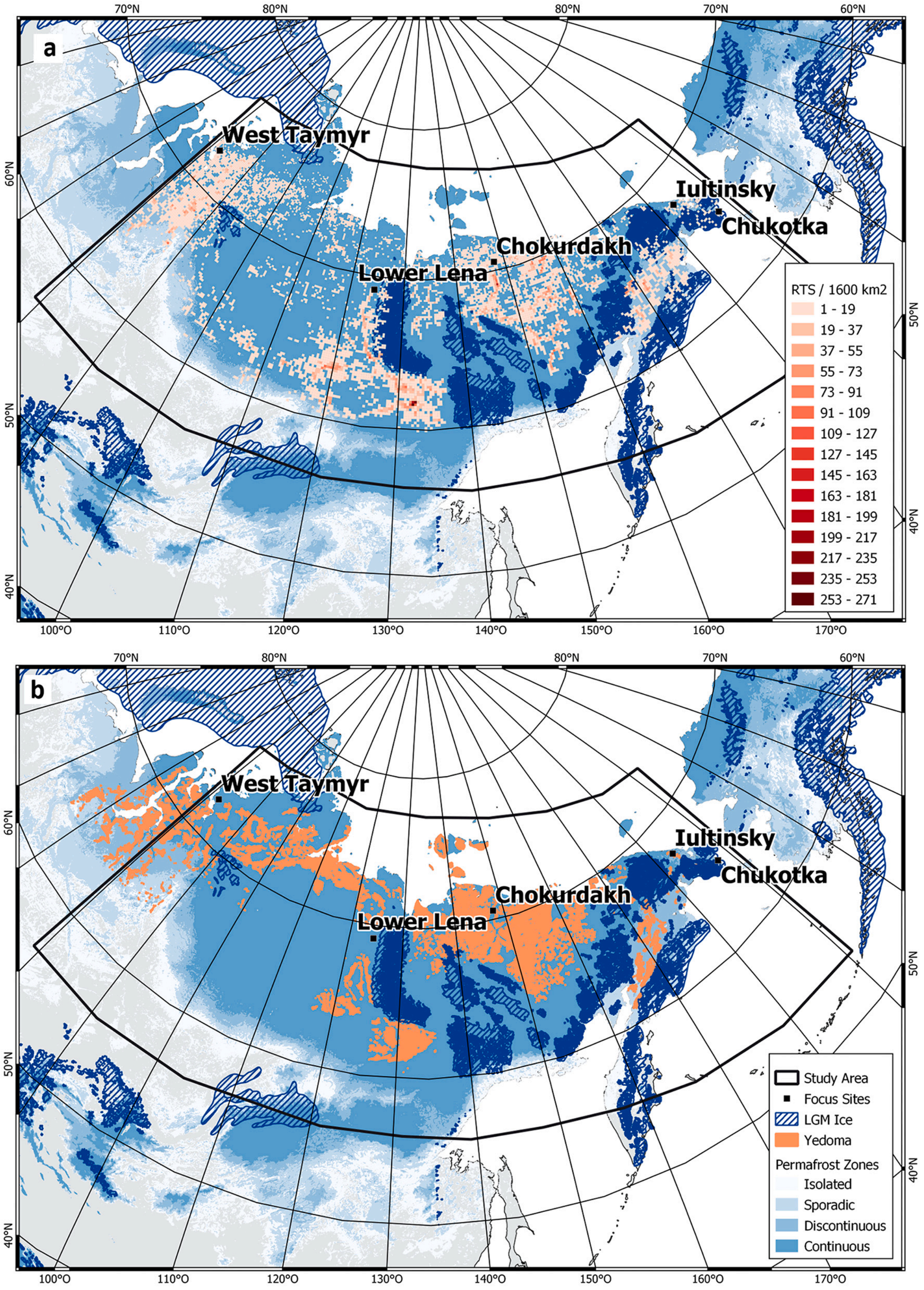

Fig. 7. a) Density map of identified RTS per $40km \times 40km$ grids in North Siberia. b) The permafrost zones are according to Obu et al. (2019), the Last Glacial Maximum (LGM) glaciation ice extent according to Ehlers and Gibbard (2003) and the Yedoma distribution according to Strauss et al. (2016).

4.2. Spatio-temporal variability of RTS dynamics

Between 2000 to 2019 we detected a steady increase in RTS-affected area for North Siberia with heightened thaw slump dynamics at the end of the observation period. Overall, the RTS-affected area increased by 331% between 2001 to 2019 (from 20,158 ha in 2000 to 66,699 ha), confirming the projected intensification and growing impact of abrupt permafrost thaw (Nitzbon et al., 2020; Turetsky et al., 2020). The majority of RTS was active at the beginning of the time series, 2000–2001, and only a smaller number of newly initiated RTS was detected in the

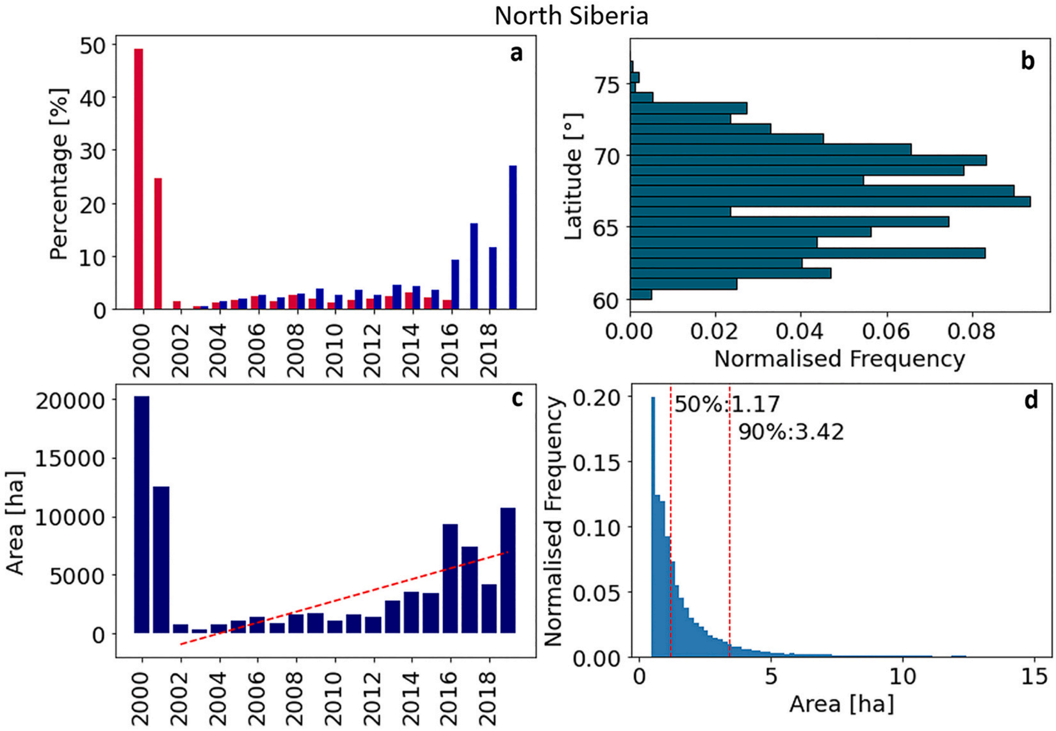

Fig. 8. Identified and mapped RTS in North Siberia: a. First year (red bar) and last year (blue bar) of RTS object activity; b. Normalised frequency of RTS by geographic latitude; c. Summarised annual RTS area [ha] with trend line indicating an increase in area from 2002 to 2019 with a slope of 374 ha per year; d. Normalised frequency of RTS object sizes.

course of the observation period. This suggests that the increase in RTS-affected area is predominantly driven by growth of existing RTS and not by initiation of new slumps, as also shown by Lewkowicz and Way (2019) for the Canadian High Arctic. However, the spatial resolution of 30 m and the applied mmu prevent to detect small-scale changes, such as RTS initiation. Therefore, we emphasise again that most likely we underestimate the number of actual RTS as well as the RTS-affected area. In contrast to this, the focus sites showed differing annual variability in the RTS thaw dynamics, indicating spatio-temporal variability of RTS thaw dynamics. All five focus sites do not show a uniform year-by-year development of RTS area but distinct periods of increased and decreased thaw dynamics. The peak slump years and periods vary between focus sites, which further confirms a strong connection to spatio-temporal varying slump drivers and environmental triggers, which lead to exposure of ice-rich ground, increased thaw, drainage and sediment transport during the thaw period. Such assessments of a high spatial variability in RTS activity and dynamics could only be addressed in limited ways by previous high temporal resolution assessments focusing more on local to regional study extents in the Canadian High Arctic or on the Qinghai-Tibet Plateau (Lewkowicz and Way, 2019; Ward Jones et al., 2019; Luo et al., 2019).

Lewkowicz and Way (2019) correlated their annual detection of growing RTS and newly initiated RTS mainly to warm summer years on Banks Island. A similar relationship was found by Ward Jones et al. (2019) for their Canadian High Arctic study sites on Ellesmere and Axel Heiberg Islands. Besides this, Kokelj et al. (2015) linked increased slumping activity to heavy precipitation events and downward sediment fluxes for the more southern study area of the Peel Plateau, in NW Canada. All these studies point towards a strong correlation between climatic and environmental drivers and RTS activity. Following this, we correlated the yearly affected RTS area of the focus sites to climate variables. We derived the mean temperature, the total annual precipitation, the total precipitation for July and August and the number of thawing days from ERA5 reanalysis data (C3S, 2017). However, we found no significant correlation between these climate variables and the annual RTS area, but only varying tendencies for the different focus sites. Lewkowicz and Way (2019) and Kokelj et al. (2015) pointed out a temporal lag of one or two years between the occurrence of reinforcing thaw drivers and actual increased permafrost thaw and RTS development. Therefore, a closer analysis of possible climate drivers and annual RTS dynamics is required to identify the spatio-temporal RTS drivers at the different focus sites, but this is outside the scope of this study.

Overall, combining the results from the focus sites and North Siberia, we can imply that the steady increase in RTS-affected area in North Siberia results from spatio-temporal variability of RTS thaw dynamics at local to regional scale. This emphasises the heightened relevance of abrupt permafrost disturbances at the large-scale but without underestimating the importance of local to regional assessments when it comes, for example, to infrastructure planning or other site-specific analyses. The impact of advancing permafrost degradation by rapid RTS development on local-scale is very pronounced in changing topographic gradients, hydrological systems, and biogeochemical cycling and can largely be considered irreversible. Most numerical permafrost models do not yet include rapid thaw processes. However, in a recent modeling study for the cold and ice-rich permafrost regions of Northeast Siberia, which were previously thought to remain largely stable despite gradual warming, Nitzbon et al. (2020) included thermokarst dynamics and found the landscape to be considerably affected by permafrost degradation already by 2100. Current carbon models also show that by 2300 abrupt permafrost thaw disturbances will occur on less than 20% of the permafrost region, but their carbon contribution will be of global relevance due to their rapid and deep erosion of ice-rich permafrost (Turetsky et al., 2020). The combination of this high carbon release potential and the abrupt and widespread thaw process by RTS, also discovered in this assessment for North Siberia, make RTS a highly important disturbance feature.

4.3. LT-LS2 capabilities and limitations

LT-LS2 identifies disturbances from temporal segmentation of spectral trajectories. The accuracy of the temporal segmentation showed that the progression of the year-to-year thaw dynamics of RTS are captured well (Table 8), with an estimated year of disturbance accuracy of ±2 years (Section 2.9). Yet, this correlation varies and depends on good quality input data as seen for few GT transects. By using medoid mosaics combining both Landsat and Sentinel-2 we enhanced the input database greatly (Runge and Grosse, 2020), similarly to approaches for MODIS time series ingesting both Aqua and Terra images (Sulla-Menashe et al., 2014). However, even Landsat and Sentinel-2 mosaics might not succeed in providing full spatial and temporal coverage in cloud-prone areas, such as northern coastal and high Arctic areas. Besides this, Sentinel-2 images are only available since 2016 for Siberia and before that we rely on Landsat-only mosaics. Thus, we assessed a possible correlation between input data and affected RTS area. For the focus sites we derived the average number of cloud-free pixels for each year, which is an indicator for the input mosaic quality as the likelihood of obtaining consistent and gap-free mosaics increases with the number of cloud-free pixels. Although the number of clear pixels increased drastically with Sentinel-2 in 2016 for all focus sites, we did not find a correlation between the average yearly clear-pixel count and identified RTS-affected area. This suggests that there is no bias between detected RTS area and enhanced mosaic coverage at the end of the time series, but it rather implies reliable disturbance detection throughout the assessment period. This is in contrast to findings from a study on cropland change, where the image availability and detection of cropland changes showed a correlation (Dara et al., 2018). However, cropland changes and abandonment are gradual changes, which are further distorted by land cover phenology and outliers that are more likely and pronounced in low quality input mosaics (Dara et al., 2018). Compared to this, the detection of RTS disturbances is based on determining and extracting the biggest disturbance segment, following abrupt, drastic spectral change. This method is more robust to shifts in phenology and outliers, which might arise in Landsat-only mosaics in years with few cloud-free images and affirms reliable disturbance detection also for the first 15 years in the time series.

Insecurities on the definite year of disturbance identification remain with a deviation of approximately ±2 years. While this lowers the confidence for explicit year of disturbance associations, the 20-year time series assessment is still able to depict peak periods of abrupt thaw. Furthermore, the accuracy of the annual dynamics is affected by the 30 m spatial resolution of the input data. Small-scale initial disturbances of only a few meters width will not be captured by 30 m spatial resolution, which will result in a delay of detecting RTS initiation and early growth and is therefore considered a low-resolution bias (Sulla-Menashe et al., 2014). A delay of detection can further be perpetuated by thaw slumping processes where the vegetation cover and hence the spectral land cover reflectance remains intact while the soil column already subsides or erodes underneath. Contrary to this, the identification of a disturbance can be premature if other changes precede the RTS disturbance, such as vegetation change, active layer detachment slides or flooding of lake or river shores.

In spite of the reliable detection of temporal RTS dynamics with LT-LS2 at local-scale, the application at large-scale required further attention as we encountered high commission errors. The spectral-temporal segmentation included a variety of false positives, such as remnants of fire scars, lake change and drainage, changing water levels and sediment transport in rivers, shadows in mountains and other commissions. The difficulty to detect and map RTS at large-scale and to separate from false positives has been discussed before (Nitze et al., 2018). Manual RTS confirmation was possible at the focus sites but not for the large-scale North Siberian application. Hence, a rigorous post-classification of the identified disturbance objects was necessary to reduce the amount of false positives and narrow the analysis to RTS disturbances. Considering that RTS are very local, small-scale features, the amount of training and validation data, compared to the false positives was very low and sparsely scattered across North Siberia as qualitative VHR data is only infrequently available for North Siberia. Also, prior studies of detailed local RTS assessments are very sparse in this large study region (e.g., Séjourné et al., 2015; Günther et al., 2016). This sparseness in high-resolution data decreases the LT-LS2 RTS classification accuracy to a F1 score of 0.609 for RTS. At the same time, the LT-LS2 classification reduced the overall number of identified disturbance objects drastically. We are confident that final RTS mapping and analysis of RTS across North Siberia, represents a reasonable and fitting framework for a first large-scale assessment at high temporal resolution. However, we cannot completely rule out the false inclusion of fire scar remnants, multi-year active layer detachment slides or regular landslides, or other disturbance artefacts as indicated by the classification accuracy.

The RTS distribution and density map indicates local and regional RTS clusters, closely related to climatic, geologic and topographic conditions. The use of VHR imagery and assessment methods can therefore now be regionally targeted and used for a high spatial resolution assessment of RTS in the future, provided the availability of VHR data. Multi-sensor constellations such as RapidEye and PlanetScope acquire images at increased rates and high spatial resolution, which increases the likelihood of obtaining high quality images. This could confirm and narrow the identified RTS objects in conjunction with the high temporal resolution assessment presented here as well as enhance the identification of initiation and small-scale changes. So far, the long time series of high temporal high spatial resolution cannot be replaced by VHR data but a combination of both will enhance the detection of small-scale changes. Similarly, the development of new improved mapping methods, such as deep learning algorithms, may help achieving a high mapping accuracy. For example, RTS in Tibet were mapped using deep learning techniques with CubeSat images at high spatial resolution, which ensured a more accurate estimation of RTS-affected area but is currently still limited to local study sites and only short assessment periods (Huang et al., 2020).

5. Conclusion

Our study includes the adaptation of the LandTrendr algorithm to capture the rapid permafrost disturbance dynamics of RTS at high temporal resolution in a first large-scale assessment across North Siberia. Parametrisation of LT-LS2 by extending the data input to Landsat and Sentinel-2, adjustment of the temporal segmentation, adaptation of the spectral and spatial masking parameters, and a binary machine-learning classification allowed us to identify and map RTS. While ground truth is sparse, we aimed to thoroughly assess and parametrise the individual workflow steps with available VHR data, resulting in a reliable and robust assessment framework for high temporal RTS analysis. Our assessment showed an overall steady increase in RTS-affected area in the $8.1 \times 10^6 km^2$ study area and highlights the abundance and rapid dynamics of abrupt permafrost thaw processes in ice-rich permafrost landscapes. Local focus-site assessments indicated spatio-temporal variability of RTS thaw dynamics. These patterns and year-by-year processes can only be detected at high temporal resolution and would be missed by low temporal resolution assessments and trend analysis. It is apparent that RTS do not develop uniformly but are caused by varying drivers. The data set with annual resolution of RTS thaw dynamics now allows for a detailed assessment of thaw slumping drivers. Our study covered heterogeneous permafrost regions with varying climatic, geologic, geomorphological and vegetation conditions, which are also common in other regions of the pan-arctic. In our rather short time series covering 20 years (2000–2019), we observed an increasing impact of abrupt permafrost disturbances on the landscape. Considering that numerical models project increasing permafrost thaw due to climate change and strong Arctic warming also in very ice-rich permafrost regions, we assume that this observed trend will further continue.

Code and data products

The LT-LS2 RTS disturbance data set will be provided on PANGAEA archive for public access.

Funding

This work was supported by BMBF KoPf (03F0764B), BMBF KoPf Synthesis (03F0834B), ESA GlobPermafrost, ESA CCI+ Permafrost, HGF AI-CORE, NSF Permafrost Discovery Gateway (1927920), and RapidEye Science Archive (RESA) (Thaw Dynamics of Retrogressive Thaw Slumps from High Resolution Images in Siberia (RTStrendr)).

Declaration of Competing Interest

The authors declare the following financial interests/personal relationships which may be considered as potential competing interests: Alexandra Runge reports equipment, drugs, or supplies was provided by RapidEye Science Archive (RESA). Alexandra Runge reports financial support was provided by BMBF KoPf (03F0764B). Alexandra Runge reports financial support was provided by BMBF KoPf Synthesis (03F0834B). Alexandra Runge reports financial support was provided by ESA GlobPermafrost. Ingmar Nitze reports financial support was provided by HGF AI-CORE. Ingmar Nitze reports financial support was provided by NSF Permafrost Discovery Gateway (1927920). Ingmar Nitze reports financial support was provided by ESA CCI Permafrost.

Acknowledgments

We thank Sophia Barth (AWI) for delineating RTS extents, Cornelia Zygar (AWI) for a first framework for LandTrendr parametrisation, and Ulrike Herzschuh and Birgit Heim (both AWI) for constructive discussions of this research. Lastly, we thank Google for providing access to the Google Earth Engine resources and R. Kennedy and his team for providing the original LandTrendr algorithm and thorough documentation. Lastly, we thank the editors and the anonymous reviewers for their time and valuable input to this manuscript. We acknowledge support by the Open Access Publication Funds of Alfred-Wegener-Institut Helmholtz-Zentrum für Polar- and Meeresforschung.

Appendix A

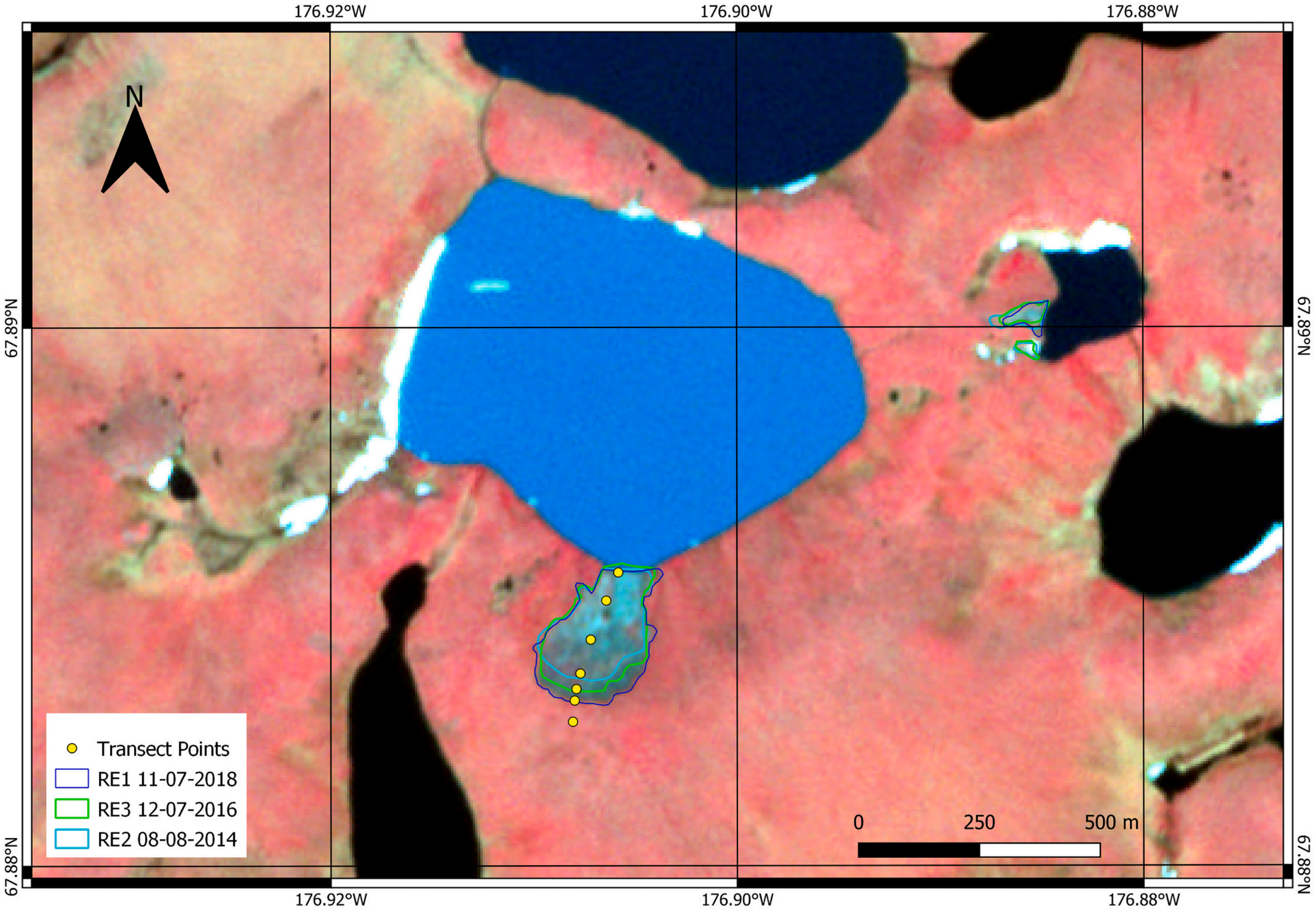

Fig. A.9. The RTS extents at different years and determined observation transect points for an exemplary retrogressive thaw slump on a lake in Iultinsky. The base picture is a false-colour composite of the RapidEye image RE1 11-07-2018. Bluish color of the lake indicates substantial sediment influx from the RTS as opposed to other dark lakes in the surrounding.

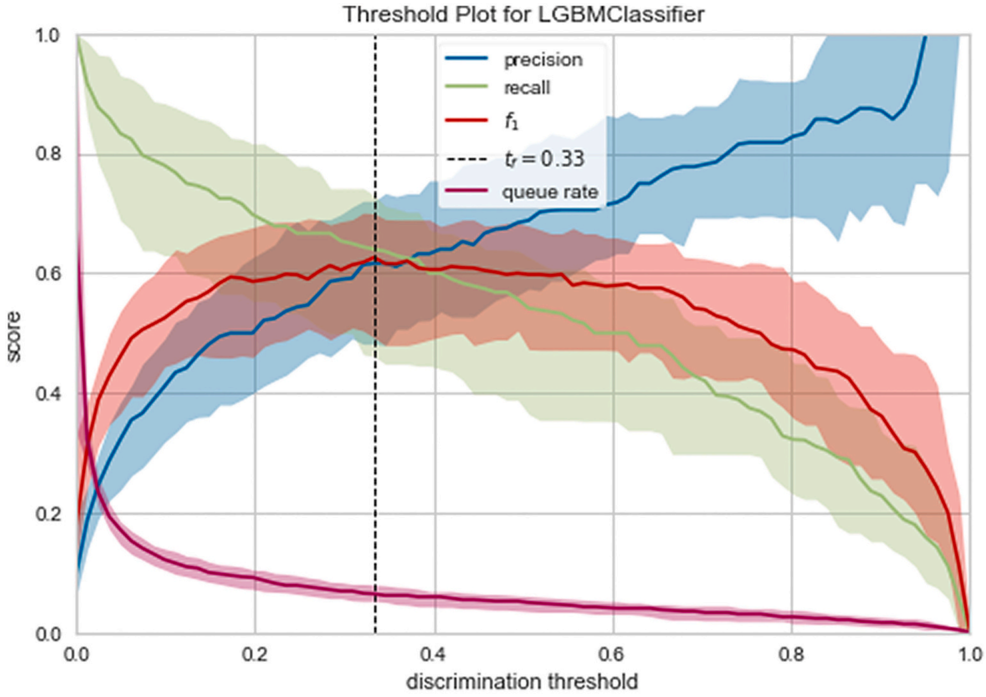

Fig. A.10. "Threshold" estimator in pycaret for the classification model.

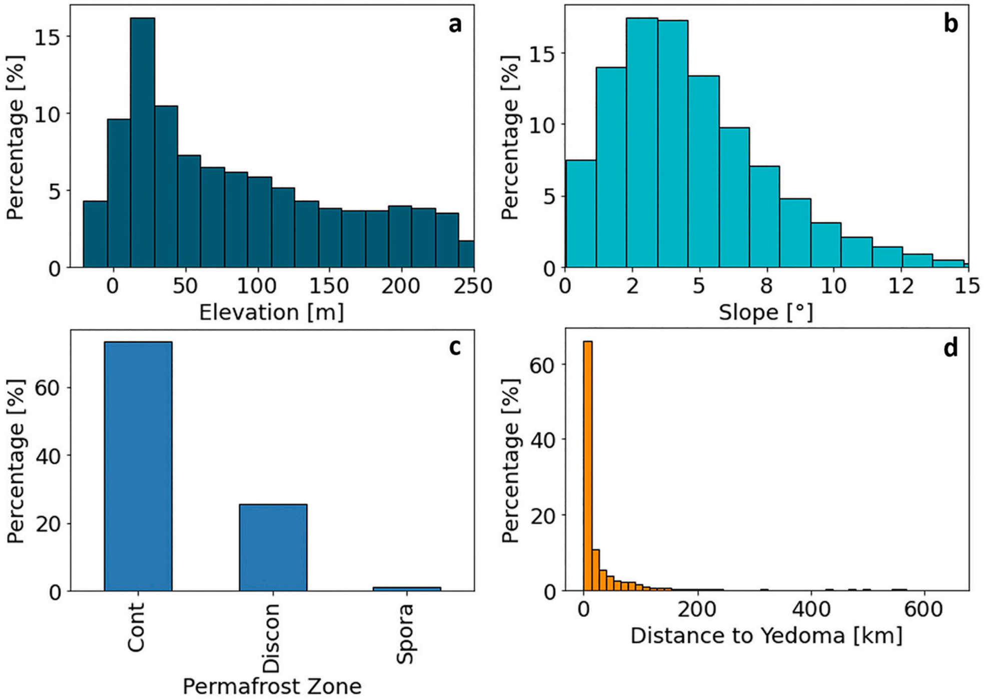

Fig. A.11. Geo-location assessment of mapped RTS in North Siberia. The percentage of RTS a. according to elevation, b. according to slope (both Porter et al. (2021)), c. according to permafrost zone (Obu et al., 2019), and d. according to distance to Yedoma (Strauss et al., 2016).

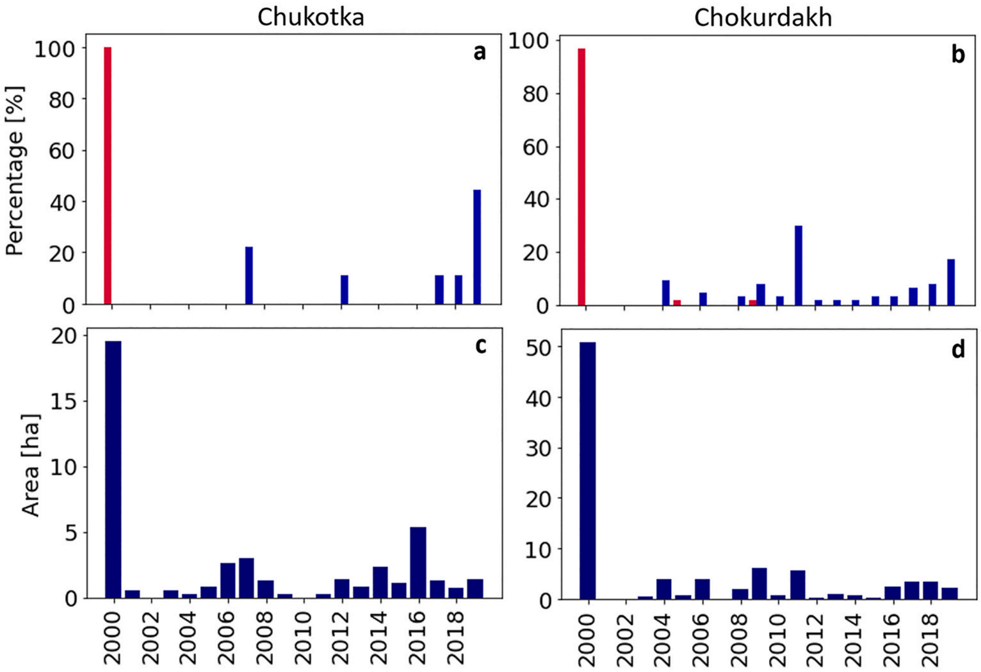

Fig. A.12. Specific results of RTS dynamics for the focus sites Iultinsky, Lower Lena, and West Taymyr.

References

Ali, M., 2020. PyCaret: An open source, low-code machine learning library in Python. URL: https://www.pycaret.org pyCaret version 2.3.

Ardelean, F., Onaca, A., Che?an, M.A., Dornik, A., Georgievski, G., Hagemann, S., Timofte, F., Berzescu, O., 2020. Assessment of spatio-temporal landscape changes from VHR images in three different permafrost areas in the Western Russian Arctic. Remote Sens. 12, 3999.

Are, F.E., 1988. Thermal abrasion of sea coast. Polar Geogr. Geol. 12, 1–157.

Balser, A.W., Jones, J.B., Gens, R., 2014. Timing of retrogressive thaw slump initiation in the Noatak Basin, northwest Alaska, USA. J. Geophys. Res. Earth Surf. 119, 1106–1120.

Barr, I.D., Clark, C.D., 2012. An updated moraine map of Far NE Russia. J. Maps 8, 431–436.

Biskaborn, B.K., Smith, S.L., Noetzli, J., Matthes, H., Vieira, G., Streletskiy, D.A., Schoeneich, P., Romanovsky, V.E., Lewkowicz, A.G., Abramov, A., et al., 2019. Permafrost is warming at a global scale. Nat. Commun. 10, 264.

Box, J.E., Colgan, W.T., Christensen, T.R., Schmidt, N.M., Lund, M., Parmentier, F.J.W., Brown, R., Bhatt, U.S., Euskirchen, E.S., Romanovsky, V.E., et al., 2019. Key indicators of Arctic climate change: 1971–2017. Environ. Res. Lett. 14, 045010.

Brooker, A., Fraser, R.H., Olthof, I., Kokelj, S.V., Lacelle, D., 2014. Mapping the activity and evolution of retrogressive thaw slumps by tasselled cap trend analysis of a Landsat satellite image stack. Permafr. Periglac. Process. 25, 243–256.

Brown, J., Ferrians Jr., O.J., Heginbottom, J.A., Melnikov, E.S., 1997. Circum-Arctic map of Permafrost and Ground-Ice Conditions. US Geological Survey Reston, VA.

Burn, C.R., Lewkowicz, A.G., 1990. Canadian landform examples-17 retrogressive thaw slumps. Canadian Geographer/Le Géographe canadien 34, 273–276.

Cassidy, A.E., Christen, A., Henry, G.H.R., 2017. Impacts of active retrogressive thaw slumps on vegetation, soil, and net ecosystem exchange of carbon dioxide in the Canadian High Arctic. Arct. Sci. 3, 179–202.

Chawla, N.V., Bowyer, K.W., Hall, L.O., Kegelmeyer, W.P., 2002. SMOTE: synthetic minority over-sampling technique. J. Artif. Intell. Res. 16, 321–357.

Cohen, W.B., Yang, Z., Kennedy, R., 2010. Detecting trends in forest disturbance and recovery using yearly Landsat time series: 2. TimeSync-Tools for calibration and validation. Remote Sens. Environ. 114, 2911–2924.

Copernicus Climate Change Service (C3S), 2017. ERA5: Fifth Generation of ECMWF Atmospheric Reanalyses of the Global Climate. Copernicus Climate Change Service Climate Data Store (CDS). Accessed March 2021.

Dara, A., Baumann, M., Kuemmerle, T., Pflugmacher, D., Rabe, A., Griffiths, P., Hölzel, N., Kamp, J., Freitag, M., Hostert, P., 2018. Mapping the timing of cropland abandonment and recultivation in northern Kazakhstan using annual Landsat time series. Remote Sens. Environ. 213, 49–60.

Ehlers, J., Gibbard, P.L., 2003. Extent and chronology of glaciations. Q. Sci. Rev. 22, 1561–1568.

ESRI, 2017. ESRI Satellite [basemap], 29-June-2017. Accessed 15-February-2021.

Farquharson, L.M., Romanovsky, V.E., Cable, W.L., Walker, D.A., Kokelj, S.V., Nicolsky, D., 2019. Climate change drives widespread and rapid thermokarst development in very cold permafrost in the Canadian High Arctic. Geophys. Res. Lett. 46, 6681–6689.

Flood, N., 2013. Seasonal composite Landsat TM/ETM+ images using the medoid (a multi-dimensional median). Remote Sens. 5, 6481–6500.

Grosse, G., Harden, J., Turetsky, M., McGuire, A.D., Camill, P., Tarnocai, C., Frolking, S., Schuur, E.A.G., Jorgenson, T., Marchenko, S., Romanovsky, V., Wickland, K.P., French, N., Waldrop, M., Bourgeau-Chavez, L., Striegl, R.G., 2011. Vulnerability of high-latitude soil organic carbon in North America to disturbance. J. Geophys. Res. Biogeosci. 116.

Grosse, G., Jones, B., Arp, C., 2013. Thermokarst lakes, drainage, and drained basins. In: Shroder J.F., Giardino, R., Harbor, J. (Eds.), Treatise on Geomorphology. Academic Press, San Diego, CA, pp. 325–353 volume 8.

Günther, F., Grosse, G., Jones, B.M., Schirrmeister, L., Romanovsky, V.E., Kunitsky, V., 2016. Unprecedented permafrost thaw dynamics on a decadal time scale: batagay mega thaw slump development, Yana Uplands, Yakutia, Russia. In: AGU Fall Meeting Abstracts.

Günther, F., Grosse, G., Wetterich, S., Jones, B.M., Kunitsky, V.V., Kienast, F., Schirrmeister, L., 2015. The Batagay Mega Thaw Slump, Yana Uplands, Yakutia, Russia: Permafrost thaw Dynamics on Decadal Time Scale. TERRA NOSTRA-Schriften der GeoUnion Alfred-Wegener-Stiftung.

Günther, F., Overduin, P.P., Sandakov, A.V., Grosse, G., Grigoriev, M.N., 2013. Short-and long-term thermo-erosion of ice-rich permafrost coasts in the Laptev Sea region. Biogeosciences 10, 4297–4318.

Hansen, M.C., Potapov, P.V., Moore, R., Hancher, M., Turubanova, S.A., Tyukavina, A., Thau, D., Stehman, S.V., Goetz, S.J., Loveland, T.R., et al., 2013. High-resolution global maps of 21st-century forest cover change. Science 342, 850–853.

Hicks Pries, C.E., Van Logtestijn, R.S.P., Schuur, E.A.G., Natali, S.M., Cornelissen, J.H.C., Aerts, R., Dorrepaal, E., 2015. Decadal warming causes a consistent and persistent shift from heterotrophic to autotrophic respiration in contrasting permafrost ecosystems. Glob. Change Biol. 21, 4508–4519.

Hjort, J., Karjalainen, O., Aalto, J., Westermann, S., Romanovsky, V.E., Nelson, F.E., Etzelmüller, B., Luoto, M., 2018. Degrading permafrost puts Arctic infrastructure at risk by mid-century. Nat. Commun. 9, 1–9.

Huang, C., Wylie, B., Yang, L., Homer, C., Zylstra, G., 2002. Derivation of a tasselled cap transformation based on Landsat 7 at-satellite reflectance. Int. J. Remote Sens. 23, 1741–1748.

Huang, L., Luo, J., Lin, Z., Niu, F., Liu, L., 2020. Using deep learning to map retrogressive thaw slumps in the Beiluhe region (Tibetan Plateau) from CubeSat images. Remote Sens. Environ. 237, 111534.

Jorgenson, M.T., Grosse, G., 2016. Remote Sensing of landscape change in permafrost regions. Permafr. Periglac. Process. 27, 324–338.

Justin, B., 2020. LandTrendr Time Series Animator.

Kanevskiy, M., Shur, Y., Fortier, D., Jorgenson, M.T., Stephani, E., 2011. Cryostratigraphy of late Pleistocene syngenetic permafrost (Yedoma) in Northern Alaska, Itkillik River exposure. Quat. Res. 75, 584–596.

Ke, G., Meng, Q., Finley, T., Wang, T., Chen, W., Ma, W., Ye, Q., Liu, T.Y., 2017. Lightgbm: A highly efficient gradient boosting decision tree. In: Guyon, I., Luxburg, U.V., Bengio, S., Wallach, H., Fergus, R., Vishwanathan, S., Garnett, R. (Eds.), Advances in Neural Information Processing Systems. Curran Associates, Inc.

Kelso, N.V., Patterson, T., 2010. Introducing natural earth data-naturalearthdata. com. Geographia Technica 5, 25.

Kennedy, R.E., Yang, Z., Cohen, W.B., 2010. Detecting trends in forest disturbance and recovery using yearly Landsat time series: 1. LandTrendr-temporal segmentation algorithms. Remote Sens. Environ. 114, 2897–2910.

Kennedy, R.E., Yang, Z., Gorelick, N., Braaten, J., Cavalcante, L., Cohen, W.B., Healey, S., 2018. Implementation of the LandTrendr algorithm on Google Earth Engine. Remote Sens. 10, 691.

Key, C.H., Benson, N.C., 2005. Landscape Assessment: Remote Sensing of Severity, the Normalized Burn Ratio and Ground Measure of Severity, the Composite Burn Index. FIREMON: Fire Effects Monitoring and Inventory System Ogden. USDA Forest Service, Rocky Mountain Res. Station, Utah.

Kokelj, S.V., Jenkins, R.E., Milburn, D., Burn, C.R., Snow, N., 2005. The influence of thermokarst disturbance on the water quality of small upland lakes, Mackenzie Delta region, Northwest Territories, Canada. Permafr. Periglac. Process. 16, 343–353.

Kokelj, S.V., Jorgenson, M.T., 2013. Advances in thermokarst research. Permafr. Periglac. Process. 24, 108–119.

Kokelj, S.V., Lacelle, D., Lantz, T.C., Tunnicliffe, J., Malone, L., Clark, I.D., Chin, K.S., 2013. Thawing of massive ground ice in mega slumps drives increases in stream sediment and solute flux across a range of watershed scales. J. Geophys. Res. Earth Surf. 118, 681–692.

Kokelj, S.V., Lantz, T.C., Kanigan, J., Smith, S.L., Coutts, R., 2009. Origin and polycyclic behaviour of tundra thaw slumps, Mackenzie Delta region, Northwest Territories, Canada. Permafr. Periglac. Process. 20, 173–184.

Kokelj, S.V., Lantz, T.C., Tunnicliffe, J., Segal, R., Lacelle, D., 2017. Climate-driven thaw of permafrost preserved glacial landscapes, northwestern Canada. Geology 45, 371–374.

Kokelj, S.V., Tunnicliffe, J., Lacelle, D., Lantz, T.C., Chin, K.S., Fraser, R., 2015. Increased precipitation drives mega slump development and destabilization of ice-rich permafrost terrain, northwestern Canada. Glob. Planet. Change 129, 56–68.

Krischke, M., Niemeyer, W., Scherer, S., 2000. Rapideye satellite based geo-information system. Acta Astronautica 46, 307–312.

Lacelle, D., Bjornson, J., Lauriol, B., 2010. Climatic and geomorphic factors affecting contemporary (1950–2004) activity of retrogressive thaw slumps on the Aklavik Plateau, Richardson Mountains, NWT, Canada. Permafr. Periglac. Process. 21, 1–15.

Lacelle, D., Brooker, A., Fraser, R.H., Kokelj, S.V., 2015. Distribution and growth of thaw slumps in the Richardson Mountains-Peel Plateau region, northwestern Canada. Geomorphology 235, 40–51.

Lantuit, H., Pollard, W.H., 2005. Temporal stereophotogrammetric analysis of retrogressive thaw slumps on Herschel Island, Yukon Territory. Nat. Hazard. Earth Syst. Sci. 5, 413–423.

Lantuit, H., Pollard, W.H., 2008. Fifty years of coastal erosion and retrogressive thaw slump activity on Herschel Island, southern Beaufort Sea, Yukon Territory, Canada. Geomorphology 95, 84–102.

Lantz, T.C., Kokelj, S.V., 2008. Increasing rates of retrogressive thaw slump activity in the Mackenzie Delta region, NWT, Canada. Geophys. Res. Lett. 35.

Lewkowicz, A.G., 2007. Dynamics of active-layer detachment failures, Fosheim Peninsula, Ellesmere Island, Nunavut, Canada. Permafr. Periglac. Process. 18, 89–103.

Lewkowicz, A.G., Way, R.G., 2019. Extremes of summer climate trigger thousands of thermokarst landslides in a High Arctic environment. Nat. Commun. 10, 1–11.

Li, J., Roy, D.P., 2017. A global analysis of Sentinel-2A, Sentinel-2B and Landsat-8 data revisit intervals and implications for terrestrial monitoring. Remote Sens. 9, 902.

Liljedahl, A.K., Boike, J., Daanen, R.P., Fedorov, A.N., Frost, G.V., Grosse, G., Hinzman, L.D., Iijma, Y., Jorgenson, J.C., Matveyeva, N., et al., 2016. Pan-arctic ice-wedge degradation in warming permafrost and its influence on tundra hydrology. Nat. Geosci. 9, 312–318.

Luo, J., Niu, F., Lin, Z., Liu, M., Yin, G., 2019. Recent acceleration of thaw slumping in permafrost terrain of Qinghai-Tibet Plateau: An example from the Beiluhe Region. Geomorphology 341, 79–85.

Morgenstern, A., Overduin, P.P., Günther, F., Stettner, S., Ramage, J., Schirrmeister, L., Grigoriev, M.N., Grosse, G., 2021. Thermo-erosional valleys in Siberian ice-rich permafrost. Permafr. Periglac. Process. 32, 59–75.

Mu, C., Shang, J., Zhang, T., Fan, C., Wang, S., Peng, X., Zhong, W., Zhang, F., Mu, M., Jia, L., 2020. Acceleration of thaw slump during 1997–2017 in the Qilian Mountains of the northern Qinghai-Tibetan plateau. Landslides 17, 1051–1062.

Nitzbon, J., Westermann, S., Langer, M., Martin, L.C., Strauss, J., Laboor, S., Boike, J., 2020. Fast response of cold ice-rich permafrost in northeast Siberia to a warming climate. Nat. Commun. 11, 1–11.

Nitze, I., Grosse, G., Jones, B.M., Romanovsky, V.E., Boike, J., 2018. Remote Sens. quantifies widespread abundance of permafrost region disturbances across the Arctic and Subarctic. Nat. Commun. 9, 1–11.

Obu, J., Westermann, S., Bartsch, A., Berdnikov, N., Christiansen, H.H., Dashtseren, A., Delaloye, R., Elberling, B., Etzelmüller, B., Kholodov, A., et al., 2019. Northern hemisphere permafrost map based on TTOP modelling for 2000–2016 at 1 km2 scale. Earth Sci. Rev. 193, 299–316.

Olson, D.M., Dinerstein, E., Wikramanayake, E.D., Burgess, N.D., Powell, G.V.N., Underwood, E.C., D'amico, J.A., Itoua, I., Strand, H.E., Morrison, J.C., et al., 2001. Terrestrial ecoregions of the world: a new map of life on Earth. Bioscience 51, 933–938.

Park, H., Kim, Y., Kimball, J.S., 2016. Widespread permafrost vulnerability and soil active layer increases over the high northern latitudes inferred from satellite remote sensing and process model assessments. Remote Sens. Environ. 175, 349–358.

Pekel, J.F., Cottam, A., Gorelick, N., Belward, A.S., 2016. High-resolution mapping of global surface water and its long-term changes. Nature 540, 418–422.

Planet Team, 2017. Planet Application Program Interface: In Space for Life on Earth, p. 40. San Francisco, CA 2017.

Porter, C., Morin, P., Howat, I., Noh, M.J., Bates, B., Peterman, K., Keesey, S., Schlenk, M., Gardiner, J., Tomko, K., Willis, M., Kelleher, C., Cloutier, M., Husby, E., Foga, S., Nakamura, H., Platson, M., Wethington, Michael, J., Williamson, C., Bauer, G., Enos, J., Arnold, G., Kramer, W., Becker, P., Doshi, A., D'Souza, C., Cummens, P., Laurier, F., Bojesen, M., 2021. ArcticDEM. Harvard Dataverse. Accessed 08-February-2021.

Quintero, N., Viedma, O., Urbieta, I.R., Moreno, J.M., 2019. Assessing landscape fire hazard by multitemporal automatic classification of Landsat time series using the Google Earth Engine in West-Central Spain. Forests 10, 518.

Ramage, J.L., Irrgang, A.M., Herzschuh, U., Morgenstern, A., Couture, N., Lantuit, H., 2017. Terrain controls on the occurrence of coastal retrogressive thaw slumps along the Yukon Coast, Canada. J. Geophys. Res. Earth Surf. 122, 1619–1634.

Rouse, J.W., Haas, R.H., Schell, J.A., Deering, D.W., et al., 1974. Monitoring vegetation systems in the Great Plains with ERTS. NASA special publication 351, 309.

Roy, D.P., Kovalskyy, V., Zhang, H.K., Vermote, E.F., Yan, L., Kumar, S.S., Egorov, A., 2016. Characterization of Landsat-7 to Landsat-8 reflective wavelength and normalized difference vegetation index continuity. Remote Sens. Environ. 185, 57–70.

Runge, A., Grosse, G., 2019. Comparing spectral characteristics of landsat-8 and sentinel-2 same-day data for Arctic-Boreal regions. Remote Sens. 11, 1730.

Runge, A., Grosse, G., 2020. Mosaicking Landsat And Sentinel-2 data to enhance LandTrendr time series analysis in northern high latitude permafrost regions. Remote Sens. 12, 2471.

Sayre, R., Karagulle, D., Frye, C., Boucher, T., Wolff, N.H., Breyer, S., Wright, D., Martin, M., Butler, K., Van Graafeiland, K., et al., 2020. An assessment of the representation of ecosystems in global protected areas using new maps of world climate regions and world ecosystems. Glob. Ecol. Conserv. 21, e00860.

Schuur, E.A., Abbott, B., 2011. High risk of permafrost thaw. Nature 480, 32–33.

Schuur, E.A.G., Mack, M.C., 2018. Ecological response to permafrost thaw and consequences for local and global ecosystem services. Ann. Rev. Ecol. Evol. Systemat. 49, 279–301.

Segal, R.A., Kokelj, S.V., Lantz, T.C., Pierce, K.L., Durkee, K., Gervais, S., Mahon, E., Snijders, M., Buysse, J., Schwarz, S., 2016. Mapping of terrain affected by retrogressive thaw slumping in Northwestern Canada. Open Report 23.

Séjourné, A., Costard, F., Fedorov, A., Gargani, J., Skorve, J., Massé, M., Mège, D., 2015. Evolution of the banks of thermokarst lakes in Central Yakutia (Central Siberia) due to retrogressive thaw slump activity controlled by insolation. Geomorphology 241, 31–40.

Stolbovoi, V., McCallum, I., 2002. Land resources of Russia. International Institute for Applied Systems Analysis and the Russian Academy of Science.

Strauss, J., Laboor, S., Fedorov, A., et al., 2016. Database of Ice-Rich Yedoma Permafrost (IRYP). PANGAEA.

Strauss, J., Schirrmeister, L., Grosse, G., Fortier, D., Hugelius, G., Knoblauch, C., Romanovsky, V., Schädel, C., Schneider von Deimling, T., Schuur, E.A., Shmelev, D., Ulrich, M., Veremeeva, A., 2017. Deep Yedoma permafrost: a synthesis of depositional characteristics and carbon vulnerability. Earth Sci. Rev. 172, 75–86.

Sulla-Menashe, D., Kennedy, R.E., Yang, Z., Braaten, J., Krankina, O.N., Friedl, M.A., 2014. Detecting forest disturbance in the Pacific Northwest from MODIS time series using temporal segmentation. Remote Sens. Environ. 151, 114–123.

Turetsky, M.R., Abbott, B.W., Jones, M.C., Walter Anthony, K., Olefeldt, D., Schuur, E.A., Grosse, G., Kuhry, P., Hugelius, G., Koven, C., et al., 2020. Carbon release through abrupt permafrost thaw. Nat. Geosci. 13, 138–143.

Turetsky, M.R., Abbott, B.W., Jones, M.C., Walter Anthony, K., Olefeldt, D., Schuur, E.A., Koven, C., McGuire, A.D., Grosse, G., Kuhry, P., et al., 2019. Permafrost Collapse is Accelerating Carbon Release.

Ulrich, M., Matthes, H., Schirrmeister, L., Schütze, J., Park, H., Iijima, Y., Fedorov, A.N., 2017. Differences in behavior and distribution of permafrost-related lakes in Central Yakutia and their response to climatic drivers. Water Resour. Res. 53, 1167–1188.

Vasiliev, A.A., Drozdov, D.S., Gravis, A.G., Malkova, G.V., Nyland, K.E., Streletskiy, D.A., 2020. Permafrost degradation in the Western Russian Arctic. Environ. Res. Lett. 15, 045001.

Van der Walt, S., Schönberger, J.L., Nunez-Iglesias, J., Boulogne, F., Warner, J.D., Yager, N., Gouillart, E., Yu, T., 2014. scikit-image: image processing in Python. PeerJ 2, e453.

Walter Anthony, K., von Deimling, T.S., Nitze, I., Frolking, S., Emond, A., Daanen, R., Anthony, P., Lindgren, P., Jones, B., Grosse, G., 2018. 21st-century modeled permafrost carbon emissions accelerated by abrupt thaw beneath lakes. Nat. Commun. 9, 3262.

Ward Jones, M.K., Pollard, W.H., Jones, B.M., 2019. Rapid initialization of retrogressive thaw slumps in the Canadian High Arctic and their response to climate and terrain factors. Environ. Res. Lett. 14.

Wilson, E.H., Sader, S.A., 2002. Detection of forest harvest type using multiple dates of Landsat TM imagery. Remote Sens. Environ. 80, 385–396.

Wulder, M.A., Loveland, T.R., Roy, D.P., Crawford, C.J., Masek, J.G., Woodcock, C.E., Allen, R.G., Anderson, M.C., Belward, A.S., Cohen, W.B., et al., 2019. Current status of Landsat program, science, and applications. Remote Sens. Environ. 225, 127–147.

Yang, Y., Erskine, P.D., Lechner, A.M., Mulligan, D., Zhang, S., Wang, Z., 2018. Detecting the dynamics of vegetation disturbance and recovery in surface mining area via Landsat imagery and LandTrendr algorithm. J. Clean. Prod. 178, 353–362.

Zhu, Z., 2017. Change detection using Landsat time series: a review of frequencies, preprocessing, algorithms, and applications. ISPRS J. Photogram. Rem. Sens. 130, 370–384.